University Hospital of Ulm
Institute of General Physiology
Director: Prof. Dr. med. Paul Dietl

A New Tool for Live Cell Imaging during Uni-axial Stretch or Compression and Its Application on Single Pneumocytes

Dissertation
To Obtain the Doctoral Degree of Medicine (Dr. med.)
at the Faculty of Medicine, University of Ulm

Axel Gerstmair
born in Sindelfingen

2008

Present Dean:	Prof. Dr. Klaus-Michael Debatin
1st Reviewer:	Prof. Dr. med. Paul Dietl
2nd Reviewer:	Prof. Dr. med. vet. Anita Ignatius
Graduation Day:	17.12.2009

Contents

List of Abbreviations

AM	acetoxymethyl ester
ANOVA	analysis of variance
AT I	alveolar type one (cell)
AT II	alveolar type two (cell)
ATP	adenosine tri-phosphate
BW	body weight
$[Ca^{2+}]_i$	intracellular calcium concentration
CO_2	carbon dioxide
CPU	central processing unit
CSA	cell surface area
DC	direct current
DMEM	Dulbecco's Modified Eagle's Medium
DMSO	dimethylsulfoxide
DNase	deoxyribonuclease
ECM	extracellular matrix
EDTA	ethylene diamine tetraacetic acid
EGTA	ethylene glycol tetraacetic acid
FBS	fetal bovine serum
FRAP	fluorescence recovery after photobleaching
FRET	fluorescence resonance energy transfer
GUI	graphical user interface
HEPES	4-(2-hydroxyethyl)-1-piperazineethanesulfonic acid
IDE	integrated development environment
IgG	Immunoglobulin G
IO	input/output
IRDS	infant respiratory distress syndrome

LB	lamellar body
MSA	membrane surface area
PBS	phosphate buffered saline
PC	personal computer
RFU	relative fluorescence units
RGB	red, green, blue
ROI	region of interest
SD	standard deviation
SEM	standard error of mean
SP	surfactant protein, i.e. SP-A, SP-B, SP-C, and SP-D
Tris	tris-(hydroxymethyl)-aminomethane
TRP	transient receptor potential
TRPC	transient receptor potential, canonical sub-family
TRPV	transient receptor potential, vanilloid sub-family
USB	Universal Serial Bus
UV	ultraviolet

Chapter 1

Introduction

Playing an important role in tissue and cell physiology, mechanical forces influence many aspects of the cell, like behavior, structure, and differentiation, but can also lead to diseases. In the lung, breathing—and even more so gasping and yawning—puts stress on epithelial cells and deforms them (Tschumperlin and Margulies, 1999; Liu et al., 1999b; Wirtz and Dobbs, 2000) resulting in various signals and responses, one of which is evidently the exocytotic secretion of surfactant (Clements, 1997; Mason and Voelker, 1998; Dietl et al., 2004), involving a transient rise of intracellular calcium concentration ($[Ca^{2+}]_i$) (Wirtz and Dobbs, 1990; Haller et al., 1999; Ashino et al., 2000; Frick et al., 2004). Exocytosis of surfactant by alveolar type two (AT II) cells has been studied for many years, however, elucidating the intricate intracellular signal cascades and extracellular interactions is very challenging and calls for a variety of examination methods. Here, we have developed a new method for investigating cells under application of uniaxial stretch at a high temporal and spatial resolution and tested it on AT II cells, focusing on transient $[Ca^{2+}]_i$ increases and surfactant secretion.

1.1 Alveolar Type II Cells and Surfactant Secretion

Alveolar epithelial cells form alveoli, the terminal and smallest units of the respiratory tree, which belong to the respiratory zone and act as the primary site of gas exchange with the blood (Fig. 1). Whereas alveolar type one (AT I) cells are flat and extensive, accounting for most of the alveolar surface and being responsible for the gas exchange, AT II cells are small and cuboidal and have several functions, for example, they produce and secrete surfactant, a phospholipid that reduces alveolar surface tension, and

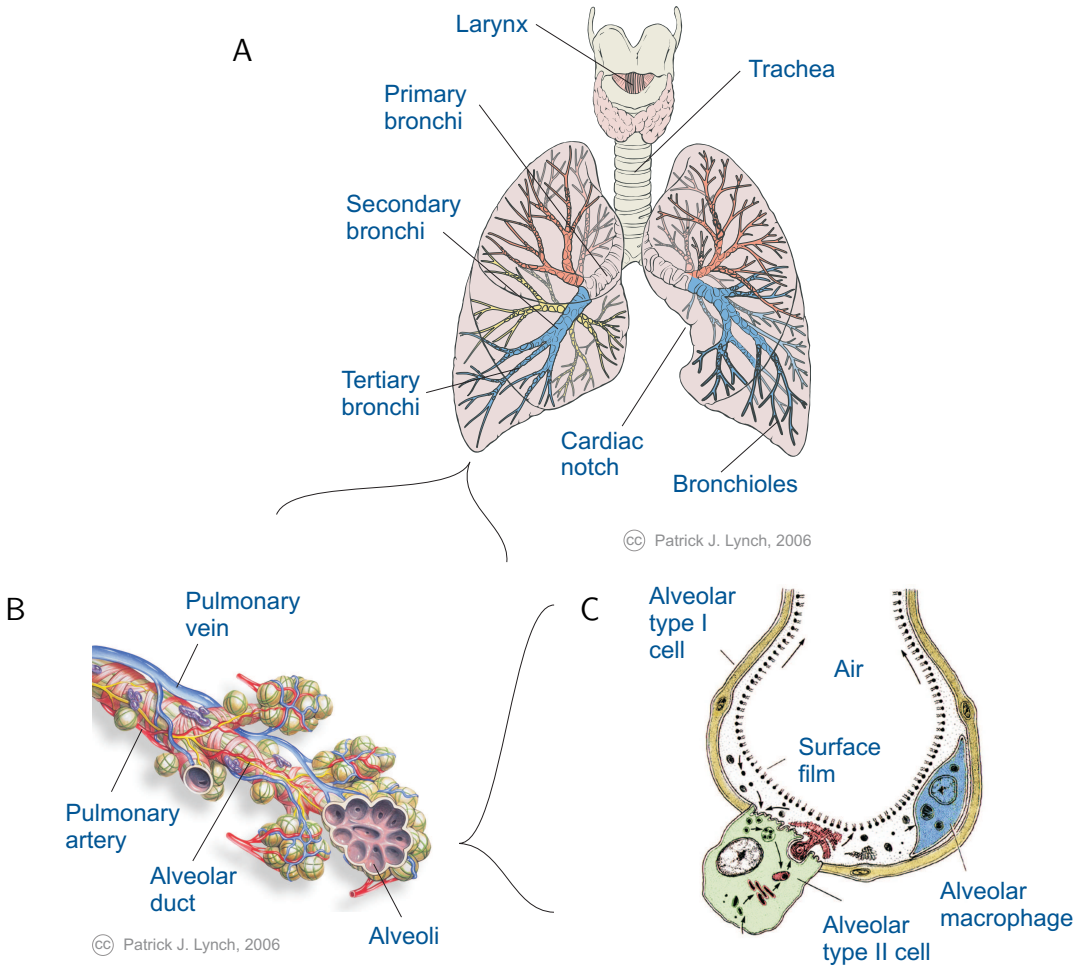

Figure 1 Anatomy of the respiratory tract. A gives an overview of the respiratory airways with the lungs being drawn transparent to allow the bronchi to be seen. B: A magnified view shows the smallest units of the bronchial tree—the alveolar ducts and alveoli. C is a schematic of an alveolus and illustrates the different cell types and their arrangement. (A, B by courtesy of Patrick J. Lynch; C modified from Hawgood and Clements, 1990)

contribute to the regeneration of the alveolar epithelium.

Pulmonary surfactant is composed of a mixture of lipids and specific surfactant proteins (SP-A, SP-B, SP-C, and SP-D) and is stored in and secreted from intracellular vesicles called lamellar bodies (LB) (Clements, 1997; Dietl et al., 2004). The exocytotic process is slow and it can take seconds to hours from stimulation to secretion. In the alveolar lumen, surfactant forms a film that is partially recycled by reuptake from AT II cells (Dietl and Haller, 2005; Wright and Clements, 1987). Surfactant is vital and its deficiency at birth causes respiratory failure as part of the infant respiratory distress syndrome (IRDS) (Avery and Mead, 1959; Engle and Committee on Fetus and

Newborn, 2008), whereas in children and adults, surfactant dysfunction can lead to or appear with other pulmonary diseases.

Lamellar bodies are acidic vesicles related to the late lysosome (Wadsworth et al., 1997; Dietl and Haller, 2005) and their fusion with the plasma membrane of the AT II cell, which can be detected by FM1-43 fluorescence as established by Haller et al. (1998), represents the endpoint of surfactant exocytosis. Hence, these fusion events serve as a valuable indicator for many experiments.

1.2 Cellular Mechanotransduction

Sensing, converting, and generating mechanical forces in living cells involves intricate interactions of various structural elements and dynamic processes and has been studied extensively (Liu et al., 1999b; Bao and Suresh, 2003; Vlahakis and Hubmayr, 2003; Huang et al., 2004; Ingber, 2006). The process of converting physical forces into biochemical signals and integrating these signals into the cellular responses is referred to as mechanotransduction (Huang et al., 2004). Figure 2 gives an overview of components

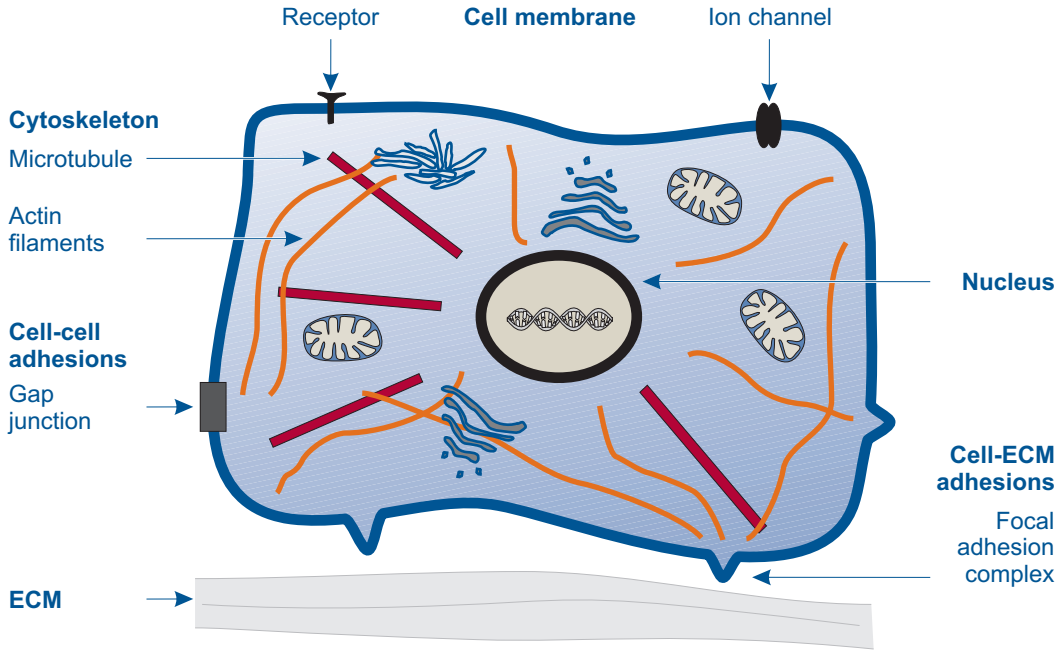

Figure 2 Components of cellular mechanotransduction in an eucaryotic cell. Many components from single molecules to complex intra- and extracellular structures are involved in mechanotransduction including the cell membrane, the cytoskeleton, cell-cell adhesions, extracellular matrix (ECM), cell-ECM adhesions, and the nucleus (categories shown in bold).

contributing to mechanotransduction at the cellular level. Interactions at the cell-cell and cell-matrix borders are transmitted to the internal cellular structures (Felder et al., 2008), such as the actin filaments of the cytoskeleton, and can affect the nucleus and ultimately gene expression. Thereby focal adhesions—large, dynamic protein complexes that link the cytoskeleton to the extracellular matrix (ECM)—and integrins—cell surface receptors interacting with the ECM—evidently play an important role (Ingber, 2003; Hu et al., 2003). But there are also other elements like mechanosensitive ion channels that are located in the cell membrane and that can convert mechanical stimuli into an influx of calcium ions, which again activates other signaling cascades. Two mechanisms have been proposed for the activation of mechanosensitive channels: first, by direct activation via tension generation in the lipid bilayer, and second, indirectly via tension in the cytoskeleton (Hayakawa et al., 2008).

Combining research in this area with other fields, Ingber proposes the notion of tensionally integrated systems of mechanochemical control (Ingber, 2003, 2006), where a cell—with its actin cytoskeleton, microtubule struts, and ECM adhesions—exists in a state of isometric tension on which external forces are imposed. Such a model may help to explain the interaction and role of the many components that are involved, because of the complex nature of cellular mechanotransduction, however, in this study we focus on a single aspect: the role of $[Ca^{2+}]_i$ changes, keeping mechanosensitive ion channels in mind for further studies.

1.2.1 Calcium Mobilization and Lamellar Body Exocytosis

An increase in intracellular calcium level is a stimulus for many cellular responses and, as Wirtz and others have shown, it plays also an important role in exocytosis of lung surfactant by AT II cells (Wirtz and Dobbs, 1990; Haller et al., 1999; Frick et al., 2004). Mechanical strain, for example, a single stretch, can elicit a transient rise of $[Ca^{2+}]_i$ in AT II cells, which originates either from intracellular stores or from extracellular fluid, and increases the likelihood of LB fusions. Although it remains unclear which mechanism causes the $[Ca^{2+}]_i$ rises, mechanosensitive ion channels, in particular channels from the transient receptor potential (TRP) family, have been proposed as potential candidates.

TRP channels are cation channels comprising a large family (over 30 types) (Clapham et al., 2001; Christensen and Corey, 2007). They are classified into seven subfamilies, of which TRPC (canonical), TRPV (vanilloid), and TRPM (melastatin) are best known. The role of many channels has yet to be determined, however, some members of the

TRPC and TRPV subfamily are expressed in lung cells and can be activated by mechanical forces (Nilius et al., 2004; O'Neil and Heller, 2005; Hamanaka et al., 2007). Hence, they present themselves as an interesting target for future research of mechanotransduction in AT II cells.

1.3 Cell-Stretching Devices

Many custom-made and some commercially available devices exist for applying a mechanical stimulus to single cells or groups of cells in vitro (Brown, 2000; Bader and Knight, 2008). A common approach is to grow the cells of interest on a flexible membrane that has been coated with molecules of the ECM, like collagen or fibronectin (Dallas et al., 2006), or synthetic substrates, like poly-lysine (Yavin and Yavin, 1974; Mazia et al., 1975), to facilitate cell adhesion. Together with the attached cells, the membrane, usually a silicone elastomer, can be subjected to various types of deformation (Fig. 3). Depending on tissue and cell type, it is desirable to mimic a specific kind of tensional forces as they occur physiologically, for example, unidirectional stretch when investigating endothelial cells (Naruse et al., 1998), striated muscle cells (Zhuang et al., 2000; Iwata et al., 2003), or axonal damage (Pfister et al., 2003). Therefore, many devices have been built to suit specific purposes and although their list is long, the number of employed mechanisms is limited (Liu et al., 1999b; Huang et al., 2004), for example, linear actuators or pistons used to generate uniaxial strain, O-rings and indenters for biaxial strain, and vacuum and pressure pumps for miscellaneous applications. Table 1 gives an overview of various cell-stretching devices and their mode of operation.

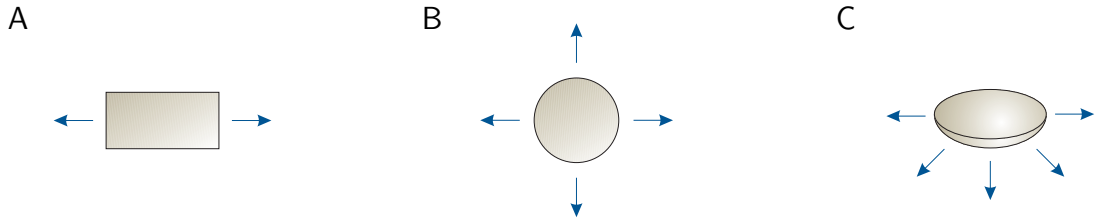

Figure 3 Strain types. Mechanical forces can be applied in various ways to an elastic membrane and cells attached to it. A: Uniaxial or unidirectional strain is the simplest form; two forces are pulling at the sides in opposite direction. B: When forces are acting both in axial and transverse direction, i.e. in x and y direction, without shear stress, the strain type is called biaxial or equibiaxial, if their absolute value is equal. C: Application of triaxial strain results in a deformation of all three spatial dimensions, for example, when inflating a balloon.

Table 1 Overview of cell-stretching devices. A plus (+) or minus (−) sign in the columns "Cell culture" and "Live imaging" indicates whether the device can be deployed during cell growth in the incubator and during experiments at the microscope respectively. The list is not intended to be exhaustive.

Device/Source	Mechanism	Cell culture	Live imaging	Note
Uniaxial cell-stretching devices				
Bottlang et al. (1997)	excentric tappet and con-rod	+	−	simultaneous stretch of 6 specimens
Yost et al. (2000)	dual-rod slider, yoke, and lead screw	+	−	simultaneous stretch of 2 specimens, one side fixed
Zhuang et al. (2000)	elliptical wheel moves horizontal bars	+	−	clamps reduce transversal shrinking
Pfister et al. (2003)	voice coil linear actuator	−	+	specimen with thick upper layer reduces transversal shrinking, one side fixed
Frye et al. (2005)	piston drives mobile steel plates	+	−	one side fixed
Jungbauer et al. (2008)	excentric tappet and con-rod	−	+	
Strex ST-150 (B-Bridge International, Inc., Mountain View, CA, USA)	movable frame connected to a shaft	−	+	one side fixed
Equibiaxial cell-stretching devices				
Hung and Williams (1994)	O-ring with indenter	−	+	
Schaffer et al. (1994)	O-ring with indenter	+	−	simultaneous stretch of 6 wells
Lee et al. (1996)	O-ring with indenter	+	−	
Tschumperlin and Margulies (1998)	O-ring with indenter	−	+	simultaneous stretch of up to 9 wells
Stroetz et al. (2001)	O-ring with indenter	−	+	
Waters et al. (2001)	pneumatic actuators, cruciform membrane	+	−	anisotropic strain possible
Frick et al. (2004)	O-ring with indenter	−	+	

Table 1 Overview of cell-stretching devices (continued)

Device/Source	Mechanism	Cell culture	Live imaging	Note
Other strain devices				
Liu et al. (1999a)	Gelfoam® sponge with metal bar, deformation by magnet	+	−	three-dimensional culture of cells
Kubicek et al. (2003)	pressure-driven membrane deformation	+	−	three-dimensional strain
Tschumperlin et al. (2003)	compression by pressure	+	−	
Flexcell® StageFlexer® (Flexcell International Corp., Hillsborough, NC, USA)	vacuum pump	−	+	supports uniaxial or biaxial strain

With so many cell-stretching devices available, what justifies the development of yet another apparatus? The problem with most existing (and commercially available) cell-stretching devices is that they make live cell imaging difficult insofar as the observed area has the tendency to move out of the field of view under application of strain. This is especially true when trying to investigate an area of cells that is not located at the very center of an elastic membrane during or after stretching uniaxially. Some devices even have one side of the membrane fixed, so there is no stable position and every point on the membrane moves during stretch (Pfister et al., 2003; Strex ST-150). Based on an existing manual uniaxial cell-stretching device ("Cell Warp" by advancedLAB Singer & Frick OEG, Innsbruck, Austria), we developed a new device that addresses this problem in a simple, yet efficient way.

1.3.1 Development of a Uniaxial Cell-Stretching Device

In order to overcome the limitations of existing cell-stretching devices, the "Cell Warp" had to be motorized and mounted on a movable and likewise motorized stage. The idea was to compensate for the axial displacement of an observed area out of the field of

view by moving the stage in the opposite direction. Thus, the area under investigation would stay approximately at the same place in the field of view. The movement and synchronization of the motors is controlled by a custom-made software—as a simple open loop control by moving the membrane and stage by a specific amount in the opposite direction, depending on the original position of the observed area.

Besides the described motion compensation mechanism, the control software would allow to define arbitrary strain protocols as required by the experimental design, i.e. every protocol ranging from the usually used sinusoidal profiles to rises and falls with different slopes and to stepwise, oscillating, and even more complex profiles.

The following list sums up the advantages of the new method:

- support for real-time observations of single cells
- motion compensation of cells that are not located at the center of the membrane and, therefore, would move out of the field of view
- membrane holders support cell culture on pre-strained membranes to enable relaxation experiments
- thin, transparent silicone membranes, which allow transmitted light and fluorescence microscopy
- up to 100 % increase in membrane/cell length
- simple handling of membranes and short replacement times
- easy access to the cell under the microscope

1.4 Goals of This Study

Three primary goals were pursued in this study:

1. To establish a method for live cell imaging under application of strain. Building upon an existing manual strain device, an automated strain device with a motorized stage and appropriate control software had to be developed, which would allow the application of uniaxial strain to an elastic, transparent membrane and the simultaneous compensation of movement that is directed away from the center.

2. To test the method on type II pneumocytes. After testing and verifying the functionality of the new method in general, it had to be tested under real experimental conditions using AT II cells isolated from the rat.

3. To investigate calcium signals and LB fusion events in live AT II cells. Using high temporal and spatial resolution, various types of uniaxial cell stretch were to be applied to type II pneumocytes to examine changes in intracellular calcium concentration and exocytosis of surfactant, at the same time collecting data that is suitable for comparisons with future experiments, for example, when comparing the effects of various substances with control.

Chapter 2

Material and Methods

2.1 The Strain Device

2.1.1 Design

The motorized cell-stretching apparatus is based on the manual Cell Warp device by advancedLAB Singer & Frick OEG (Innsbruck, Austria). It has been manufactured by Innerbichler GmbH (Kundl, Austria) and adapted to our specific needs by the Wissenschaftliche Werkstatt Feinwerktechnik (scientific workshop) at the University of Ulm. Figure 4 shows a schematic drawing of the device. The cell-stretching apparatus consists of two parts that work independently of each other. The first part is the warp component which allows the application of strain to a mounted membrane. The second part is the stage component, a linear motion guide, which allows the warp component to be moved on the same axis in which the strain is applied (the x axis). Using both components together it is possible to keep an observed area at the same position during application of strain.

The warp component is made up of two blocks that slide on a linear motion guide in opposite directions and thereby determine the total length of the membrane, which is attached to the two blocks. One block is connected via a ball screw to a motor and can be moved directly. The other block is connected with the first with a spring—that pulls the blocks together—and a metal band guided around a pulley—that pulls the block in the opposite direction of the first (see the red arrows in Fig. 4). Increasing the distance between the two blocks requires an active force (the motor) whereas decreasing it follows the passive force of the spring.

The stage component is simply a plate on top of a linear motion guide (not shown

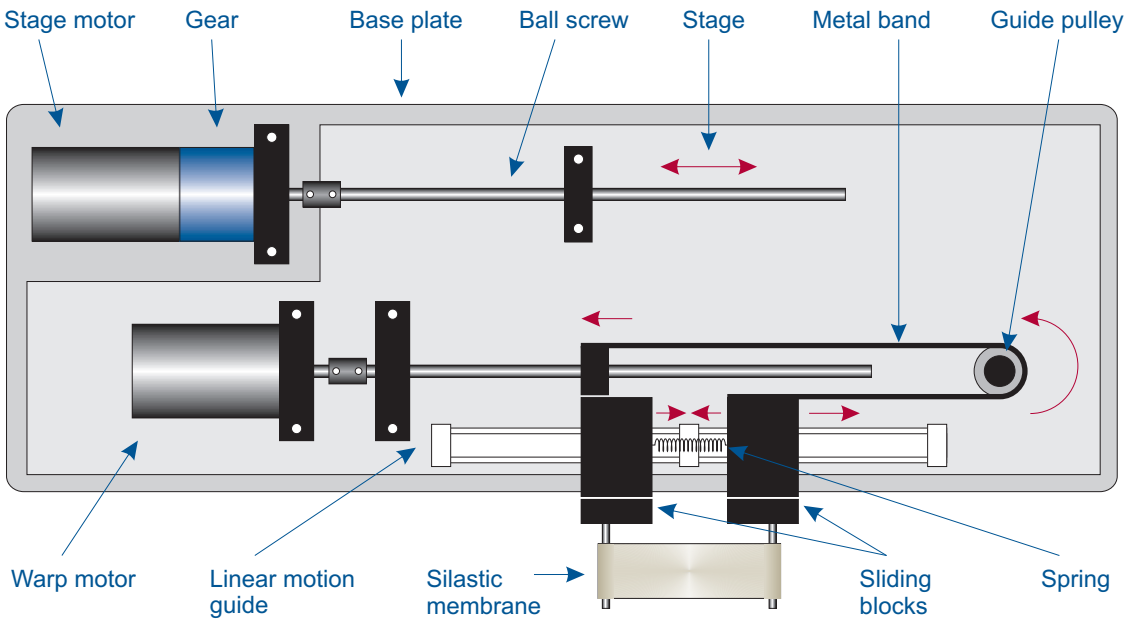

Figure 4 Schematic of the warp device. The upper part shows the stage component consisting of the stage motor, the gear, the stage (light gray), and the translational unit with the ball screw. The stage is moved by transforming the motor rotations into a linear movement. Below, the warp component, which stretches the attached membrane, is depicted. The red arrows indicate the direction of movement. See the text for more details.

in Fig. 4) that is connected via a ball screw to another motor, similarly to the warp component. All parts of the warp are attached to the plate and thus can be moved as a whole as the plate moves along the tracks.

The mechanical parts, i.e. the linear motion guides, the ball screws (with 1 mm pitch), the couplings, the guide pulley, and all the metal parts, have been supplied and assembled by Innerbichler GmbH (Kundl, Austria). Table 2 lists the components that have been used for motorizing the cell strain device. Both motors are connected to a motion controller, which again is connected to a computer using the RS-232 interface (serial port). A software then controls and coordinates the motors (see section 2.2).

Table 2 Components for motorizing the strain device

Component	Company (Location)
2 Brushless DC Servomotors 3056 K 024 B	Faulhaber (Schönaich)
Planetary Gearhead 38/1 (246:1)	Faulhaber (Schönaich)
Motion Controller MCBL 2805	Faulhaber (Schönaich)
Latitude D520 laptop	Dell GmbH (Frankfurt am Main)

2.1.2 Membranes and Membrane Chambers

In general, a very thin elastic membrane with borders serves as a chamber for seeding cells and retaining medium. Both ends of the membrane are fastened to metal rods that can be inserted into sockets at the strain device and stretch the membrane. Several kinds of membrane chambers have been used in combination with the cell strain device. They have evolved over time and, therefore, are referred to as first to third generation membrane chambers (Fig. 5).

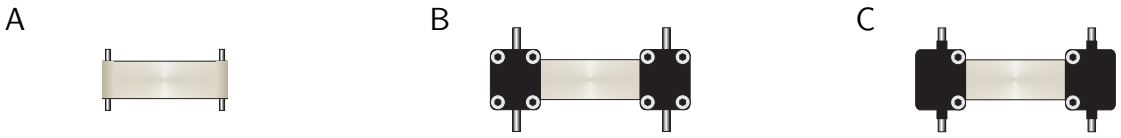

Figure 5 Membrane chambers used with the strain device. A First generation: one piece cast in a fit. The ready-made chambers have been supplied by advancedLAB Singer & Frick OEG (Innsbruck, Austria). B Second generation: a small sheet of silastic membrane is clamped by two holders and sealed with silicone at the outer edges to prevent leaking of fluids. The membrane chamber can be reused several times before its quality degrades and it has to be replaced. Building such a membrane chamber requires skill and time. C Third generation: similar to B but no sealing is necessary and the modified holders inhibit rotations. Compared to the other generations, building and handling this kind of chamber is much easier and more efficient.

The membranes used are made of an inert silicone elastomer, which provides a non-toxic environment for cells. They are very thin (127 μm) and exhibit excellent optical properties that are suited for fluorescent microscopy. Additionally, the silicone elastomer responds homogeneously to strain all-over the membrane (see section 3.1.3; Frick et al., 2004).

2.1.3 Device Calibration

For the motion compensation (see section 2.2.2) to work, it is important to know the center position of the membrane because it does not move under strain and serves as reference to all other points on the membrane (cf. Fig. 9). So the strain device has to be calibrated before doing any experiments.

For calibration of the warp and stage components, a special calibration piece is used, which is made of solid metal (nickel-plated brass) with the size of a regular silastic membrane (Fig. 6). Its extent given by the fixed distance of the rods defines zero strain, i.e. the warp component needs to move its sliding blocks until the calibration piece can be easily attached to it.

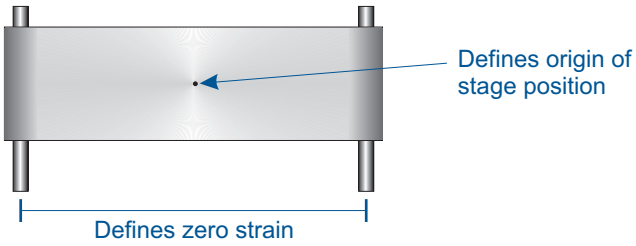

Figure 6 Schematic of the calibration piece. It is made of solid metal (nickel-plated brass) in order to avoid deformations and to allow easy handling. A very fine hole with a diameter of 0.2 mm has been drilled in the center of the metal piece and allows the microscope light to pass through.

For defining the zero position of the stage, the whole strain device with the calibration piece attached must be mounted on the microscope stage. Then the microscope stage is moved in the x and y axis until the drill hole in the center of the calibration piece, which is the only area that allows light to pass through, is centered in the field of view.

After calibration the microscope stage must not be moved in the x direction, otherwise the center position is lost and the motion compensation no longer works. In order to observe a different area on the membrane, solely the stage of the strain device must be used.

2.2 The Strain Control Software

The motorized strain device is controlled by a software that was developed from scratch only for this purpose. The strain control software is able to control both the warp and the stage component at the same time and implements a motion compensation algorithm (as described in section 2.2.2), thus stabilizing the observed area when the membrane is stretched or compressed.

The following list shows its most important features:

- controls the stage and allows to memorize stage positions, for example, to look at different interesting areas on the membrane
- controls the warp component and allows to specify a prestrain, for example, for membrane chambers that have been incubated at a certain strain and to enable compressing membranes
- allows to define arbitrary strain protocols with different types of strain (linear, sinusoidal, sigmoidal), pauses, and loops for repeating a specific sequence (cf.

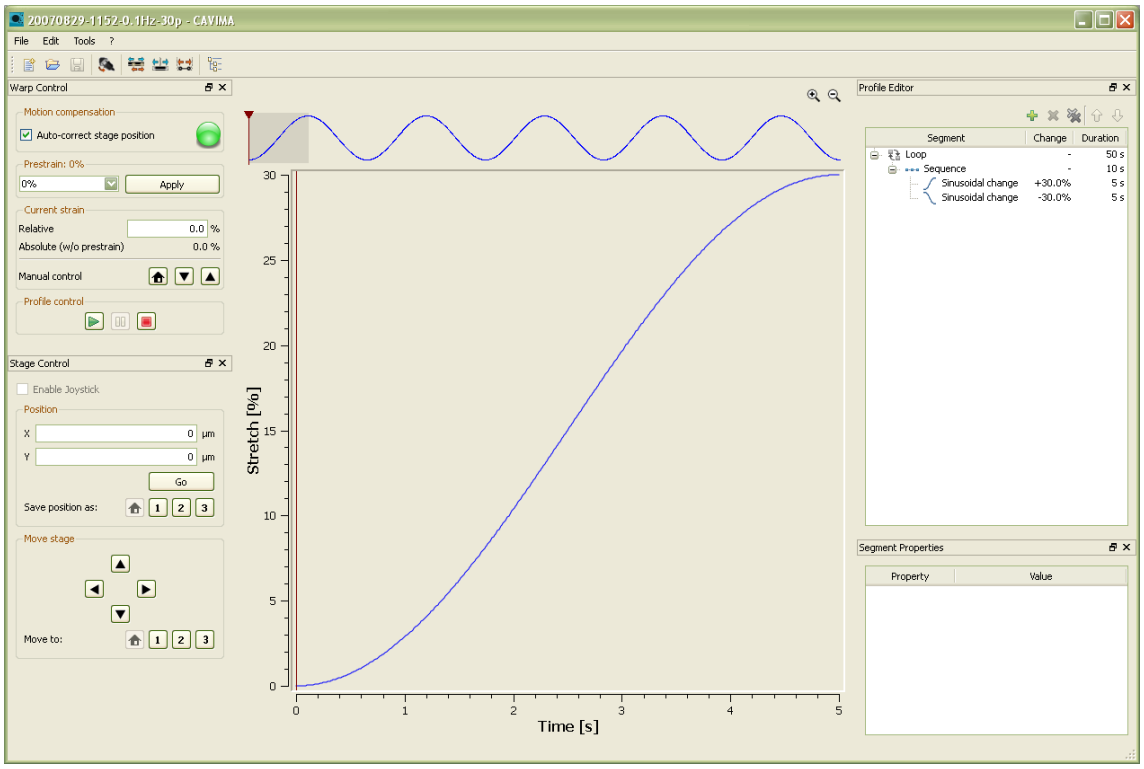

Figure 7 Screenshot of the strain control software. The graphical user interface is divided into several panels that can be arranged freely. There are separate panels for controlling the warp (upper left) and stage (lower left), for defining the warp profile (right), and for displaying the current warp profile (center).

section 2.2.1)

- supports saving and loading of strain protocols
- many parameters available to define the behavior of the cell stretching device, for example, maximum speed and acceleration

The software runs on a Dell Latitude D520 laptop that is connected to the Faulhaber motion controller via a RS-232 interface. Details about its implementation can be found in appendix B.

2.2.1 Defining Warp Profiles

Strain protocols (or warp profiles) are defined using the strain control software. A warp profile is a sequence of one or more segments that define what happens at a specific time point, e.g. a smooth increase in strain, a linear decrease or a pause. Basic

segments are represented by a shape like a linear, sinusoidal, or sigmoidal curve, the amount of change in strain, and its duration. Segments or groups of segments can be repeated, allowing to create cyclic protocols, or even nested, i.e. composing sequences of other sequences and loops, allowing to create arbitrarily complex protocols—unlike many other strain devices. Figure 8 shows examples of warp profiles.

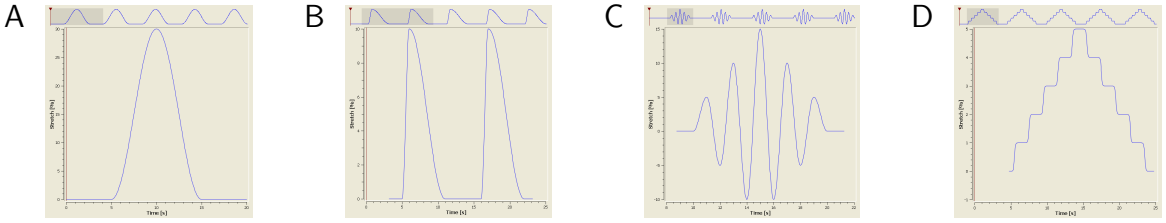

Figure 8 Example warp profiles. Using the strain control software any strain protocol can be simulated including simple sinusoidal profiles (A), profiles with different slopes (B gasping), oscillating profiles (C Cheyne-Stokes respiration), and any complex profile (D staggered).

2.2.2 Motion Compensation

In order to keep an observed point in the field of view of the microscope during application of strain it is necessary to have a model of the deformation of the membrane. Using such a model, it is then possible to predict the perceived movement of an arbitrary point on the membrane and thus to counteract the effect.

There is a simple linear correlation between the distance x_0 of an observed point from the center and the distance Δx it moves when the membrane is stretched or compressed. That is, a point at the very center of the membrane does not move. With increasing distance from the center, however, the movement becomes larger under strain (Fig. 9). Let σ be the *relative* amount of strain, where a value of 0 means no strain, values greater than 0 mean an extension of the membrane, and values less than 0 mean a compression of the membrane, then

$$\Delta x = \sigma x_0 \tag{2.1}$$

The new position x_{strain} of the observed point can then simply be obtained as

$$x_{\text{strain}} = x_0 + \Delta x \tag{2.2}$$

Now, we have determined how to calculate the amount of movement and the new position of an observed point. When looking at the problem the other way around,

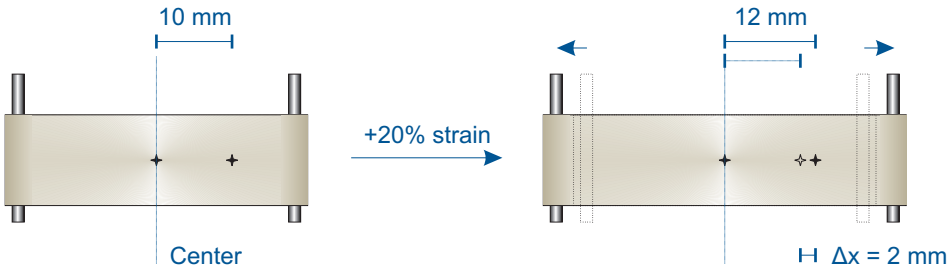

Figure 9 Strain model. The left part of the figure shows a schematic of the membrane under no strain with two positions marked (at 0 mm and 10 mm). The right part shows the same membrane under 20 % strain. It can be easily seen that the point on the center line does not move under strain whereas the second point moves 2 mm away from the center. This is due to an increase in the length of the membrane that is assumed to be distributed equally.

however, it gets a little bit more complicated. If only the position under strain is given and we want to know the original position of our observed point, we cannot simply use equation 2.1 again because the strain factor σ is relative to the original position, which is not given this time. Therefore, we must determine a different factor that considers the applied strain. At first, we have to eliminate x_0 from equation 2.2 by solving equation 2.1 for x_0 and substituting it in the former equation, which gives

$$\begin{aligned} x_{\text{strain}} &= \frac{\Delta x}{\sigma} + \Delta x \\ &= \left(\frac{1}{\sigma} + 1\right) \Delta x \\ &= \frac{1+\sigma}{\sigma} \Delta x \end{aligned} \tag{2.3}$$

Solving for Δx finally gives

$$\Delta x = \frac{\sigma}{1+\sigma} x_{\text{strain}} \tag{2.4}$$

Using equations 2.1, 2.2, and 2.4, it is possible to determine the motion under strain, relaxation, and even when moving between different levels of strain.

Membrane Deformations in Transverse Direction

Up until now, nothing was said about the deformations of the silastic membrane transverse to the strain. As the membrane is being stretched along the longitudinal axis it is being compressed in the transverse axis with the highest compression at the center of the membrane (Poisson's effect). With increasing strain in the x axis the compression in the y axis decreases.

2.3 Testing the Strain Device

2.3.1 Mounting Accuracy

To test the accuracy of the calibrated position of the cell stretching device after demounting and remounting, which is important for motion compensation, a series of measurements was performed using the motorized stage of the microscope. At first, the calibration piece was attached to the strain device, which in turn was mounted on the microscope stage. Then, the microscope stage was calibrated as described in section 2.1.3, and the the current x and y position of the stage was noted down. Last, the strain device was demounted again and the calibration piece removed. This procedure was repeated 10 times to see how much the stage position changed.

2.3.2 Stage Movement

The precision of the stage movement of the strain device and the correlation between specified and actual movement was determined by conducting a series of simple tests. After calibration of the setup, the strain device was mounted with a membrane stained either with ink of a common permanent marker or with TetraSpeck microspheres, small fluorescent beads. Then, an image was acquired and the stage position changed by a fixed amount repeating both steps 30 times, i.e. one series with steps of 1 μm, one with steps of 10 μm, and one with steps of 100 μm. Afterwards the snapshots were evaluated by tracking a salient image feature and measuring its pixel offset to the original position. Using the microscope calibration the pixel offsets were then translated into real world units (μm) and compared to the specified values.

2.3.3 Membrane Strain

Similarly to comparing specified stage movement to actual movement, tests were performed to compare specified strain with the strain that was actually measured. Again, the setup was calibrated and the strain device was mounted with a stained membrane. This time, however, the membrane was not moved but stretched in steps of 5 % up to a maximum strain of 60 %, then gradually relaxed again (back to 0 %). For each step an image was acquired, which was later evaluated by tracking three image features and measuring their relative distance in x and y direction (Fig. 10). Then, the change in distance produced the actual change in strain.

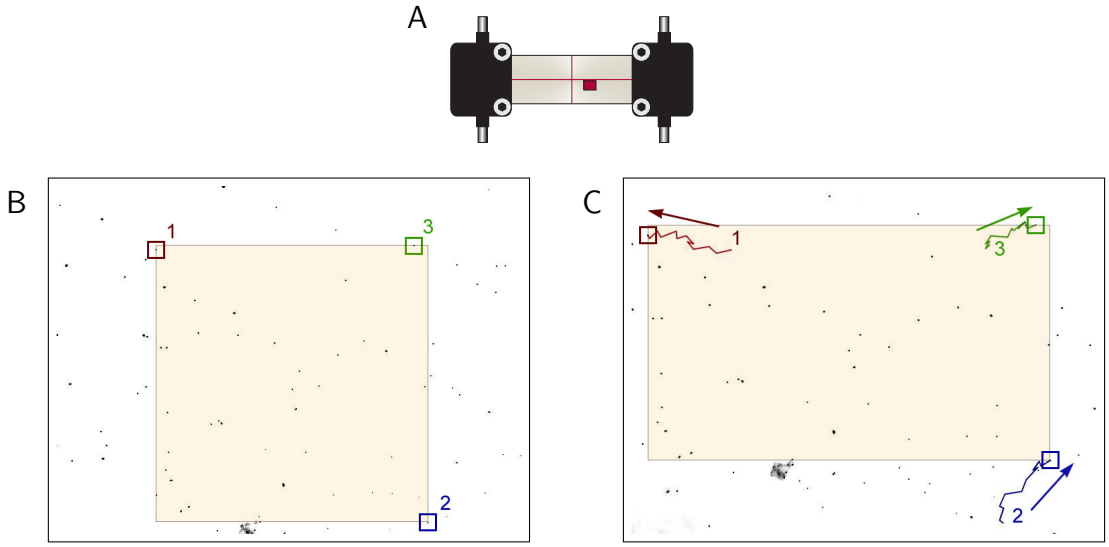

Figure 10 Example images showing tracked features at the start (B) and at 60 % strain (C). The images are taken from an experiment done with TetraSpeck microspheres, represented by the black dots, and have been inverted to facilitate presentation (white = background, black = high fluorescence). The rectangle enclosing all three tracked points determines the deformation of the membrane surface area in x and y direction. All dots on the membrane move towards the north because the observed area is a little bit off from the middle line (A) and the membrane is slightly compressed in y direction.

2.3.4 Motion Compensation

Testing the implemented motion compensation mechanism (cf. section 2.2.2) was accomplished according to the other tests by calibrating the strain device, mounting a stained membrane, and moving the stage of the strain device to a specific position. Then, turning on motion compensation, the membrane was stretched up to 50 % in steps of 1 % acquiring an image at each step. Afterwards the image series was analyzed by tracking two features, one at each side of the starting frame, and calculating the average movement of the area in the field of view. Under perfect conditions, the center of the observed area should stay at the same position during stretching. Absolute offsets were converted to percentaged error values by relating them to the specified starting position.

2.4 Cell Culture

2.4.1 Preparation of Membranes

Cleaning. A cleaning and sterilization step was performed as preparation for each experiment in order to remove debris—of a probable previous use—and microorganisms from the membrane chambers. At first, each membrane was covered with 70 % isopropanol and carefully wiped clean and dry with Q-tips repeating this process several times. Next, distilled water was repeatedly added and sucked away with a vacuum pump to remove remaining fluff and dirt. Last, the membranes were either wrapped in aluminum foil and autoclaved or treated with UV light (10 min at 100 $^{mJ}/_{cm^2}$).

Coating. Because AT II cells do not attach to and grow on the silastic membranes, the membranes had to be pretreated to facilitate the adherence. This was accomplished by a fibronectin coating. Fibronectin is a glycoprotein of the ECM that regulates cell attachment, migration, differentiation, proliferation, and survival (Dallas et al., 2006). Fibronectin stock solution (1 $^{mg}/_{ml}$) was diluted to 5 $^{\mu g}/_{ml}$ in phosphate buffered saline (PBS) with 0.75 ml of the diluted solution being pipetted on each membrane. The coating was left for at least 4 hours at 4 °C.

2.4.2 Cell Isolation

AT II cells were isolated from male Sprague Dawley rats with a body weight of 180 to 200 g according to the procedure described in Haller et al. (1998) and Dobbs et al. (1986). The surgery and isolation of cells was conducted by our technicians and cells from these preparations were used for many other experiments, too. The following sections describe the method in more detail.

Anesthesia. A solution of 0.75 ml Ketamin, 0.6 ml Rompun (Xylazine), and 1.65 ml NaCl was prepared and 3 $^{ml}/_{kg\ BW}$ intraperitoneally administered to the rat. Sometimes this dose was not sufficient to fully relax the rat, so it was necessary to inject more of the prepared solution.

Surgery. Before starting the surgery, the rat's coat was washed off with ethanol to avoid flying hair. Then the skin was incised from the abdomen to the pharynx followed by the underlying linea alba, thus opening the abdomen. The intestine was dislocated

to lay open the vena cava, which was then directly injected with heparin (400 $^{\text{IU}}/_{\text{kg BW}}$ in physiological saline). After turning the rat by 90 degrees and placing a tuberculin syringe under its neck, its trachea was dissected in a blunt way and underpinned with fine tweezers. Next, the trachea was underlaid with yarn and cut open with a small incision, inserting and securely ligating a tube. Having the infusion system prepared by filling it with preparation solution II (see table 8) and removing all air, a small hole was cut into the vena cava. Then, acting fast, the thorax was opened along the sternum and the diaphragm pierced so that the lungs collapsed. Afterwards, the diaphragm was cut through laterally and, if necessary, the thymus removed. Excising the right auricle of the heart and puncturing the left atrium, the infusion catheter was inserted into the arteria pulmonalis to perfuse the lungs with warm solution II. Simultaneously, the lungs were ventilated three times with an air-filled syringe. Then, the heart was excised and the lungs cut along the spine on their dorsal side, completely releasing them. Finally, the lungs were laid on a previously moisturized tissue and sprinkled with NaCl solution.

Washing and Enzymatic Digestion. The lungs were washed several times: 8 times with 10 ml preparation solution I (see table 7), twice with 10 ml preparation solution II (see table 8), and once with 8 ml elastase solution (see table 9, all solutions had been preheated to 37 °C). After rinsing with the elastase solution, another 5 ml were instilled and the rest of the solution left in an attached syringe. Then, the lungs were hung in a 37 °C temperated NaCl solution and incubated for 15 min. Avoiding entering of air into the lungs by pressing the trachea securely with the tube, a new syringe was attached and a total of 40 ml elastase solution was instilled—under hydrostatic pressure at about 7 cm water column over a period of 20 min. After the instillation the parenchyma was detached from the rest of the lungs, i.e. the trachea and the bronchi were discarded. Adding 1.5 ml DNase solution (2 mg), the tissue was chopped into little pieces of roughly 1 mm^3. Last, 5 ml FBS was added in order to inhibit the enzyme reaction, incubating for 2 min at 37 °C.

Filtration. For purification the suspension of lung cells was filtrated several times using different types of filters (gauze twofold → gauze twofold → gauze fourfold → 150 μm nylon mesh → 20 μm nylon mesh → 10 μm nylon mesh). The filtrate was then put into a reagent tube, filled up to a volume of 30 ml with preparation solution II, and centrifuged for 8 min at 130 g. Discarding the supernatant, the pellet was suspended

in 30 ml DMEM and dispensed onto petri dishes that had been previously coated with IgG solution (5 ml of 500 $\mu g/ml$ IgG and 50 mM Tris each, stored 3 h at room temperature). The dishes were then stored in the incubator for 15 min (at 37 °C in a 5 % CO_2 atmosphere). After incubation each petri dish was carefully rotated, then the cells were pipetted off and centrifuged again (see above). Finally, the pellet was suspended in DMEM.

2.4.3 Plating and Incubation

After removing the PBS of the fibronectin coating from the prepared membrane chambers, the previously extracted cells were plated onto the membranes (300 μl cell suspension plus 700 μl medium per membrane, see table 10). The cells were then incubated in a humidified 5 % CO_2 atmosphere for 40 to 50 hours at 37 °C.

2.4.4 Approval for Animal Experiments

The rat experiments have been approved by the Regierungspräsidium Tübingen for experimental studies on "Regulation der Surfactantfreisetzung aus Typ II Alveolarzellen der Lunge" (requested on June 21, 2005 by Prof. Dr. Paul Dietl).

2.5 Detection of Lamellar Body Fusions

In order to detect LB fusions, FM1-43 fluorescence was employed according to Frick et al. (2004, 2001); Meyers et al. (2003); Haller et al. (1998); Betz et al. (1996). The FM1-43 dye is a lipophilic styryl compound, which is cell impermeant and stains surfactant, thereby locally highlighting fusions as the LBs fuse with the plasma membrane and FM1-43 from the bath solution enters the fusion pore. In aqueous solutions the dye is non-fluorescent, which allows to add it once to the bath solution and to keep track of fusions continuously. 3 μM FM1-43 was added at the beginning of each experiment to the bath solution. Illuminating between 100 and 200 ms, FM1-43 fluorescence was recorded at a rate of 6 to 10 frames per minute depending on the duration of the experiment.

During analysis the time-lapse images acquired in the experiments were inspected for LB fusion events by marking the AT II cells in a bright field image, transferring the regions of interest to the FM1-43 image series, and scanning each region for the appearance of distinct, highly intense, circular areas demarcating fused LBs. Artifacts

like floating particles could be simply dismissed because of their movement or transient appearance, whereas fused LBs stayed put and kept their intensity over time.

2.6 Calcium Measurements

For measuring intracellular calcium ($[Ca^{2+}]_i$) levels, the well-established, UV-light excitable, ratiometric dye Fura-2 was used (Grynkiewicz et al., 1985; Roe et al., 1990; Rudolf et al., 2003) as its membrane permeable analog Fura-2 acetoxymethyl ester (AM), an acetoxymethyl ester. Fura-2 AM passes the cell membrane and, once inside, its acetoxymethyl groups are removed by intracellular esterases restoring the impermeable Fura-2 molecule. Before each experiment, 4 μM Fura-2 AM was added to the cell medium and incubated for 20 min at 37 °C. Then the medium was replaced by bath solution to remove extracellular fluorescence.

As a ratiometric dye Fura-2 undergoes a shift in maximum excitation wavelength from 380 nm to 340 nm upon binding calcium, whereas the emission maximum remains virtually unchanged at 510 nm. By calculating the ratio, confounding variables like differences in dye loading, cell thickness, and small changes in the focal plane can be diminished. Fura-2 fluorescence was recorded for both wavelengths with an exposure time of 80 ms at a rate of 6 to 10 frames per minute according to the rate of FM1-43 fluorescence acquisition. In this work, we did not calculate absolute $[Ca^{2+}]_i$ values—by calibrating and comparing with known calcium concentrations—but worked with arbitrary units and relative changes, which was sufficient to detect transient calcium peaks.

2.6.1 Data Analysis

Analysis of experimental data included image processing, feature extraction, and detection of calcium peaks.

Image Processing. For image processing the freely available software ImageJ (Rasband, 2008) was used. All time-lapse images were loaded, one image stack per acquired wavelength, and aligned due to some small shifts, which could introduce artifacts in the measurements and degrade quality. For aligning all images, both gray level stacks (at 340 nm and 380 nm wavelength) were combined into an RGB stack, which was then aligned using the Image Stabilizer plug-in (Li, 2008; Baker and Matthews, 2004; Lucas

and Kanade, 1981) calculating the best match, shifting moved images, and padding edges with black. The combination into an RGB stack assured that both image series were aligned in exactly the same way. After stabilizing the images, the RGB stack was split again into two gray level stacks allowing separate analysis. Finally, the image stacks were background subtracted using a manually selected area in order to reduce background illumination.

Feature Extraction. Using a brightfield image acquired at the beginning of each experiment as reference, the outline of each AT II cell was manually traced and saved as a region of interest (ROI). Finally, the mean intensity of each ROI, F_{340} and F_{380}, was determined for every time point and for both wavelengths resulting in a multi-column list that was exported to Microsoft Excel for further data processing.

Automated Detection of Transient Calcium Peaks. Because of the high number of observed cells (several hundred in total), the calculation of Fura-2 ratios and detection of transient calcium peaks was partially automated by creating Excel templates that accepted the raw values and returned the processed data. At first, the Fura-2 ratio $R(t)$ at time point $t = 0, 1, \ldots, t_{max}$ was determined by dividing the preprocessed, i.e. background subtracted, values of the two excitation wavelengths:

$$R(t) = \frac{F_{340}(t)}{F_{380}(t)} \tag{2.5}$$

Since a transient calcium peak represents a local maximum in the signal $R(t)$—the numerator increases as the excitation wavelength shifts to 340 nm for elevated $[Ca^{2+}]_i$—, a basic mathematical approach for local maximum detection was taken. For differentiable functions the second derivative test can be used stating that a local maximum is sufficiently described by:

$$R'(t) = 0 \quad \text{and} \quad R''(t) < 0 \tag{2.6}$$

The input signal $R(t)$, however, is not a continuous function, but is approximated by discrete values, so the condition has to be reformulated into:

$$|R'(t)| < \epsilon \quad \text{and} \quad R''(t) < 0 \tag{2.7}$$

where ϵ is a small value allowing for some tolerance in the detection of stationary points. The first and second derivative was approximated by:

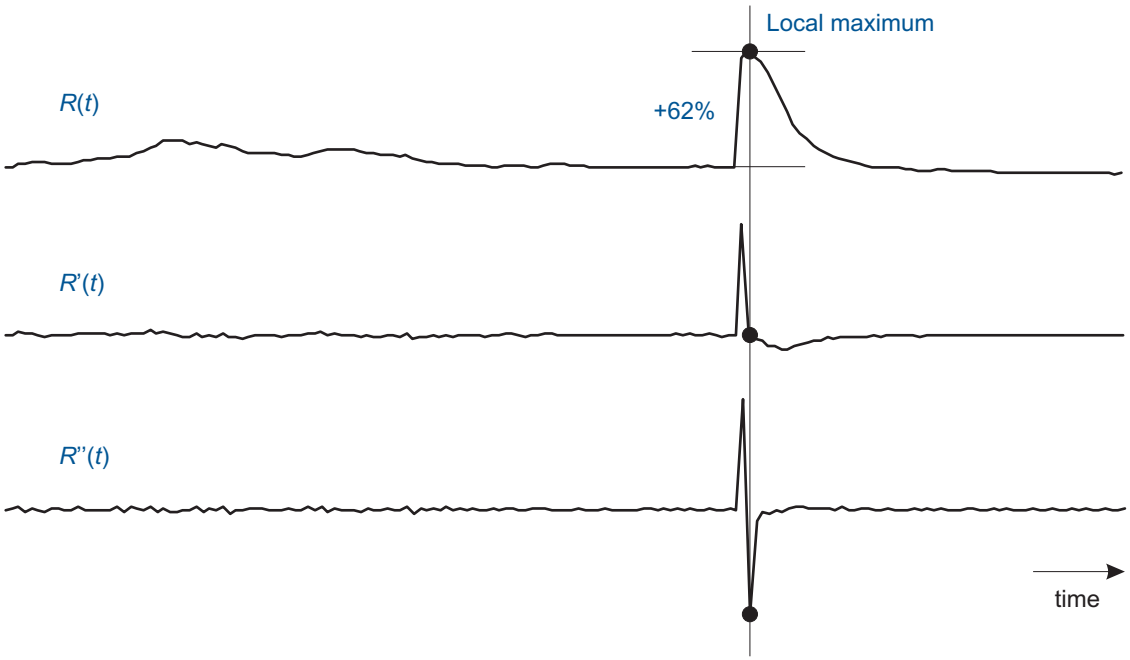

Figure 11 Detection of calcium peaks. A sample course of Fura-2 ratios $R(t)$ and its two derivatives is shown from top to bottom. A peak is characterized by a zero first derivative and a negative second derivative and its amplitude can be expressed as either an absolute value (in relative fluorescence units, RFU), by subtracting the ratio of the baseline before the peak from the ratio of the peak itself, or as a relative value (in percent), by dividing the peak value by the baseline value.

$$R'(t) = \begin{cases} 0, & t = 0 \\ R(t) - R(t-1), & t > 0 \end{cases} \tag{2.8}$$

and accordingly:

$$R''(t) = \begin{cases} 0, & t = 0 \\ R'(t) - R'(t-1), & t > 0 \end{cases} \tag{2.9}$$

Once the local maxima had been detected, the absolute and relative increase of the Fura-2 ratio with regard to the baseline before the peak was calculated for each maximum. Only peaks with a relative increase of at least 20 % were considered, dismissing all others as either noise or artifacts.

2.7 Investigations on Alveolar Type II Cells

Several series of experiments were conducted with two goals in mind: first, to test the strain device and its software under real experimental conditions, and second, to generate and analyze a data set that serves as a basis for future experiments. The tests were carried out under the same conditions varying only the strain protocol (see Fig. 12) and some minor settings like exposure times.

The following strain protocols were experimentally tested using both FM1-43 and Fura-2 fluorescence in order to simultaneously detect LB fusions and transient intracellular calcium peaks:

- controls (no strain applied)
- 20 % cyclic strain with 2 min pause
- 30 % cyclic strain with 2 min pause
- 20 % cyclic strain with 30 s pause
- 30 % cyclic strain with 30 s pause
- 10 % cyclic strain at 2 Hz with 30 s pause
- increasing amplitudes (15 %, 20 %, ..., 35 %) with 3 min pause

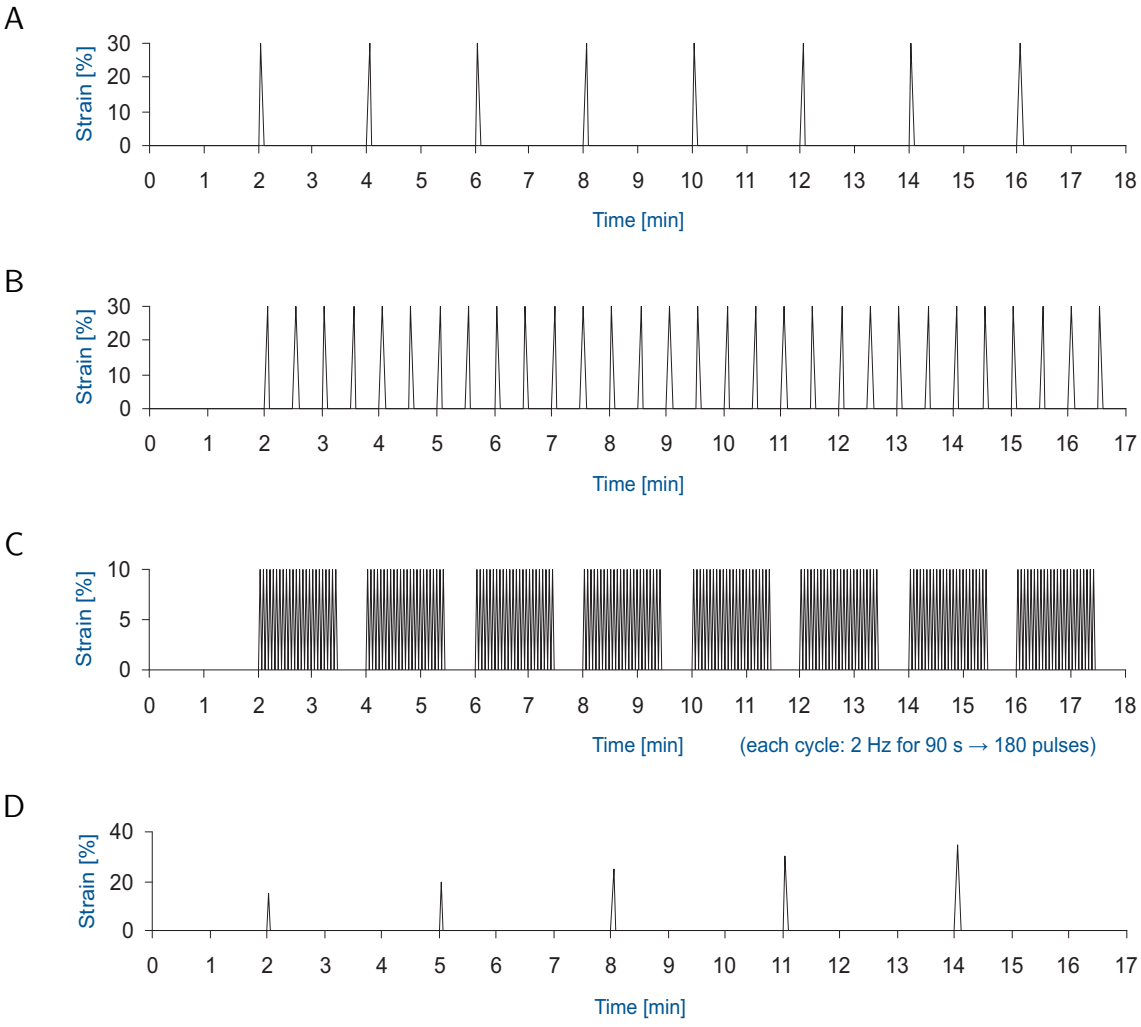

Figure 12 Experimentally tested strain protocols. A 30 % cyclic strain with 2 min pause, B 30 % cyclic strain with 30 s pause, C 10 % cyclic strain at 2 Hz with 30 s pause, D increasing amplitudes (15 %, 20 %, ..., 35 %) with 3 min pause. Strain pulses in A, B, and D were applied with a speed of 10 %/s.

In all experiments except for the cyclic strain at 2 Hz, strain pulses were applied with a speed of 10 %/s. Please note that, actually, the specified pauses are a few seconds shorter because the specified durations include the time of the strain pulse.

2.8 Equipment

2.8.1 Microscope Setup

For microscopy and fluorescence imaging a setup by Visitron Systems (Munich) was employed including the following components:

- Zeiss Axiovert 200 inverted microscope
- high accuracy Z-focus
- Prior Scientific H117E2X2 ProScan Inverted Stage (with encoders and 2 mm pitch ballscrew)
- VisiChrome Polychromator System
- Photometrics CoolSNAP EZ high-resolution camera
- highend PC workstation
- Molecular Devices MetaMorph/MetaFluor Imaging Software

Microscope calibration. The microscope and the imaging software were calibrated once using a calibration slide with marks at known intervals. Thus, a scale could be constructed that converts the pixels of the acquired images to micrometers. This was necessary for later analysis.

2.8.2 Laboratory Equipment

Table 3 Laboratory equipment

Equipment	Company (Location)
Environmental Incubator shaker	New Brunswick Scientific Co., Inc. (Edison, NJ, USA)
HERAcell® 150 CO_2 Incubator	Thermo Fisher Scientific GmbH (Dreieich)
HERAsafe® HS 15 safety cabinet	Heraeus Instruments GmbH (Hanau)
Hotplate stirrer	Bibby Scientific Ltd (Staffordshire, UK)
Membrane Vacuum Pump	Biometra biomedizinische Analytik GmbH (Göttingen)
pH-Meter CG 822	SCHOTT Instruments GmbH (Mainz)
Precision balance	Sartorius AG (Göttingen)
REAX 2000 vibrating shaker	Heidolph Instruments GmbH & Co. KG (Schwabach)
Ultraviolet Crosslinker	Amersham Life Science (Buckinghamshire, UK)
Varioklav 300 autoclave	H+P Labortechnik GmbH (Oberschleißheim)

2.9 Chemicals and Reagents

Tables 4, 5, and 6 list the chemicals, reagents, and consumables used during the experiments.

Table 4 Consumable materials

Consumable	Company (Location)
Corning®Costar®Stripettes®	Sigma-Aldrich Chemie GmbH (München)
Dishes Nunclon$^{TM}\Delta$	Nunc GmbH & Co. KG (Wiesbaden)
Non woven swabs	NOBA Verbandmittel Danz GmbH & Co. KG (Wetter)
Nylon mesh	VWR International GmbH (Darmstadt)
Reagent tubes	Sarstedt AG & Co. (Nümbrecht)
Silastic membranes (gloss/gloss finish, 127 μm)	Specialty Manufacturing, Inc. (Saginaw, MI, USA)

Table 5 Chemicals and reagents. (ATP = adenosine tri-phosphate, DMEM = Dulbecco's Modified Eagle's Medium, DMSO = dimethylsulfoxide, DNase = deoxyribonuclease, EDTA = ethylene diamine tetraacetic acid, FBS = fetal bovine serum, HEPES = 4-(2-hydroxyethyl)-1-piperazineethanesulfonic acid, IgG = Immunoglobulin G, PBS = phosphate buffered saline, Tris = tris-(hydroxymethyl)-aminomethane)

Chemical	**Company (Location)**
Acetic acid	RdH Laborchemikalien GmbH & Co. KG (Seelze)
ATP	Fluka Chemika (Buchs, Schweiz)
Bacillol®	BODE Chemie GmbH & Co. KG (Hamburg)
$CaCl_2$	Merck KGaA (Darmstadt)
DMEM	Gibco/Invitrogen (Karlsruhe)
DMSO	Fluka Chemika (Buchs, Schweiz)
DNase	Sigma-Aldrich Chemie GmbH (München)
Elastase	Elastin Products Company, Inc. (Owensville, MO, USA)
Ethanol	Universität Ulm, Klinik Apotheke (Ulm)
Fibronectin 0.1 % Solution from Bovine Plasma	Sigma-Aldrich Chemie GmbH (München)
Glucose	Merck KGaA (Darmstadt)
HCl	Merck KGaA (Darmstadt)
Heparin-Natrium Braun "Multi" 10000 $^{IU}/_{ml}$	B. Braun Melsungen AG (Melsungen)
HEPES	Sigma-Aldrich Chemie GmbH (München)
IgG from rat serum	Sigma-Aldrich Chemie GmbH (München)
Isopropanol	Universität Ulm, Klinik Apotheke (Ulm)
Isotonic sodium chloride solution	Serag-Wiessner KG (Naila)
KCl	Merck KGaA (Darmstadt)
Ketamin 10 %	WDT (Garbsen)
$MgCl_2$	Merck KGaA (Darmstadt)
NaCl	AppliChem GmbH (Darmstadt)
PBS	Biochrom AG (Berlin)
Penicillin-Streptomycin	Invitrogen Molecular Probes (Karlsruhe)
Pluronic® F-127	Invitrogen Molecular Probes (Karlsruhe)
Research Grade FBS	HyClone (Logan, UT, USA)
Rompun® 2 %	Bayer Vital GmbH (Leverkusen)
Tris	Sigma-Aldrich Chemie GmbH (München)
0.25 % Trypsin-EDTA solution	Sigma-Aldrich Chemie GmbH (München)

Table 6 Fluorescent dyes and markers

Dye/Marker	Company (Location)
Ethidium Homodimer-1	Invitrogen Molecular Probes (Karlsruhe)
Fluo-4	Invitrogen Molecular Probes (Karlsruhe)
FM1-43	Invitrogen Molecular Probes (Karlsruhe)
Fura-2 AM	Invitrogen Molecular Probes (Karlsruhe)
Hoechst 33342	Invitrogen Molecular Probes (Karlsruhe)
TetraSpeck microspheres	Invitrogen Molecular Probes (Karlsruhe)

2.9.1 Solutions and Cell Medium

Table 7 Composition of preparation solution I. Titrated to pH = 7.4.

Concentration	Component
140.0 mM	NaCl
5.0 mM	KCl
2.5 mM	phosphate buffer
10.0 mM	HEPES
6.0 mM	Glucose
0.2 mM	EGTA

Table 8 Composition of preparation solution II. Titrated to pH = 7.4.

Concentration	Component
140.0 mM	NaCl
5.0 mM	KCl
2.5 mM	phosphate buffer
10.0 mM	HEPES
2.0 mM	$CaCl_2$
1.3 mM	$MgSO_4$

Table 9 Composition of elastase solution

Concentration	Component
10 mg	Elastase
2 mg	Trypsin
40 ml	preparation solution II

Table 10 Composition of cell medium

Concentration	Component
	DMEM
1 %	Streptomycin/Penicillin
10 %	FBS

Table 11 Composition of bath solution. Titrated to pH = 7.4.

Concentration	Component
140 mM	NaCl
5 mM	KCl
1 mM	$MgCl_2$
2 mM	$CaCl_2$
5 mM	Glucose
10 mM	HEPES

2.10 Statistical Analysis

Unless noted otherwise, all results are specified as means ± standard error (SEM). Student's t-test (paired and unpaired as noted) and analysis of variance (ANOVA) were applied to test for differences in the experimental groups and a value of $p < 0.05$ was considered to be significant.

Excel 2003 (Microsoft Deutschland GmbH, Unterschleißheim) was used for pooling and grouping the data and basic statistical analysis. One-way and two-way ANOVA was performed with Matlab 6.5 (The MathWorks Deutschland, Ismaning).

Chapter 3

Results

3.1 Characterization of the Strain Device

3.1.1 Mounting Accuracy

The mounting and demounting tests showed that the position of the strain device has a standard deviation of 29.5 μm in x and 64.9 μm in y direction when re-mounting it to the microscope stage after calibration, for example, when starting a new experiment and attaching a membrane chamber to the strain device. The doubled deviation in y can be explained by the way the calibration piece is attached to the strain device and the device itself to the microscope stage—both are inserted in y direction and probably do not always reach the stop position.

3.1.2 Precision of Stage Movement

When testing the movement of the stage component of the strain device, it was found that it is strictly linearly correlated to the nominal, i.e. specified, value ($p < 0.001$, two tailed t-test). The actual position deviated from the nominal position by $-8.2\,\%$ $\pm$ 13.9 % (mean $\pm$ SD) for 1 μm steps, $+3.1\,\%$ $\pm$ 0.8 % for 10 μm steps, and $+3.0\,\%$ $\pm$ 0.7 % for 100 μm steps. Figure 13 gives a different representation, showing the actually traveled distance per step. When looking at step size 1 μm (A), the highest precision tested, it is apparent that the first one or two steps do not reach the nominal step size and that the actual step size increases minimally towards the end of the test run, suggesting a small mechanical tolerance. The results for step size 100 μm (C) show a sinusoidal curve, indicating another minor systematic error.

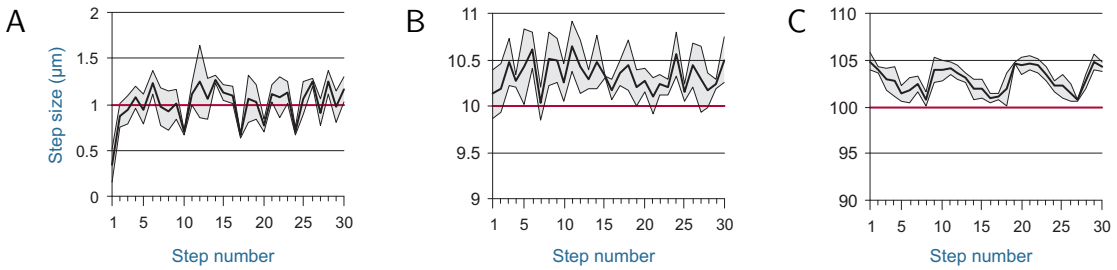

Figure 13 Precision of stage movement. The charts show the actual step size (means ± standard error of mean, $n = 3$) for all three series of movement measurements each with 30 steps of 1 μm (A), 10 μm (B), and 100 μm (C) respectively. The red line represents nominal values that are supposed to be met. Actual stage positions and, derived from them, actual step sizes were determined by acquiring high resolution images, tracking features, and converting pixel distances into real world units using the scale obtained from microscope calibration.

3.1.3 Nominal vs. Actual Membrane Strain

In order to examine how much the membranes are actually stretched when applying a specific strain, a series of tests was conducted measuring changes in membrane surface area (MSA) at different positions (Fig. 14), that is, at the center of the membrane and at two remote areas (3 tests at each position, i.e. 9 tests). When comparing the three series, it was found that the measured strain at position 3000 μm differed from strain at the center position ($p < 0.05$, two-way ANOVA, no difference between position 1000 μm and any other position), suggesting that the strain field was not strictly homogeneous over all tested areas. The absolute difference, however, is very small (48.1 % actual strain at position 3000 μm vs. 49.1 % at the center with a nominal strain of 60 %).

The same test series was analyzed for compression in transversal direction (Fig. 15) and produced a compression of 15.5 % ± 0.7 % at 60 % strain. The curve in the graph shows that compression does not increase proportionally to applied strain, but flattens with higher strain levels as expected. Additionally, position on the membrane affects the amount of compression (analogous to stretch, two-way ANOVA)—compression is highest at the center of the membrane and decreases with increasing distance until it reaches a value of zero at the edges, which are fixed.

Combining measurements of actual strain and transversal compression gives the change in MSA (Fig. 16). The relative increase in area depends linearly on specified strain, due to compression, however, amounts only to half of the specified value. For example, when a uniaxial strain amplitude of 30 % is specified, the membrane is stretched by 24.9 % ± 0.2 % (mean ± SEM) in axial direction, compressed by 9.5 % ± 0.4 % in transversal direction, and therefore enlarged by 13.0 % altogether.

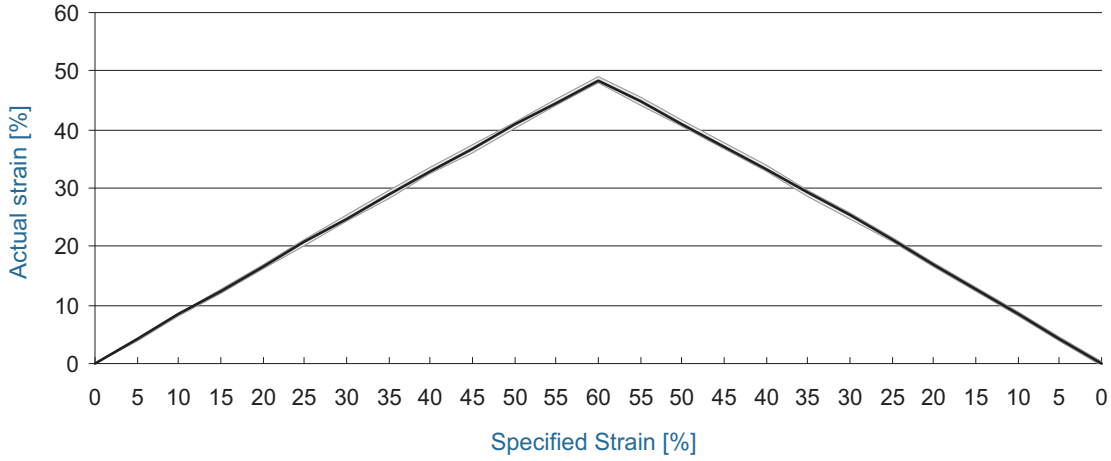

Figure 14 Actual strain in axial direction. After moving to a specific position (0 μm, 1000 μm, and 3000 μm respectively, relative to the center, $n = 3$ for each), a stained membrane (only second and third generation, cf. section 2.1.2) was stretched up to 60 % in steps of 5 %. For each step, the change in membrane surface area was determined by tracking at least two image features and measuring their relative distances resulting in a width and height that could be compared to the initial values at zero strain. The actual strain is less than the specified strain and deviates by -12 % at 60 % strain. The curve shows the means of all experiments $\pm$ standard deviation.

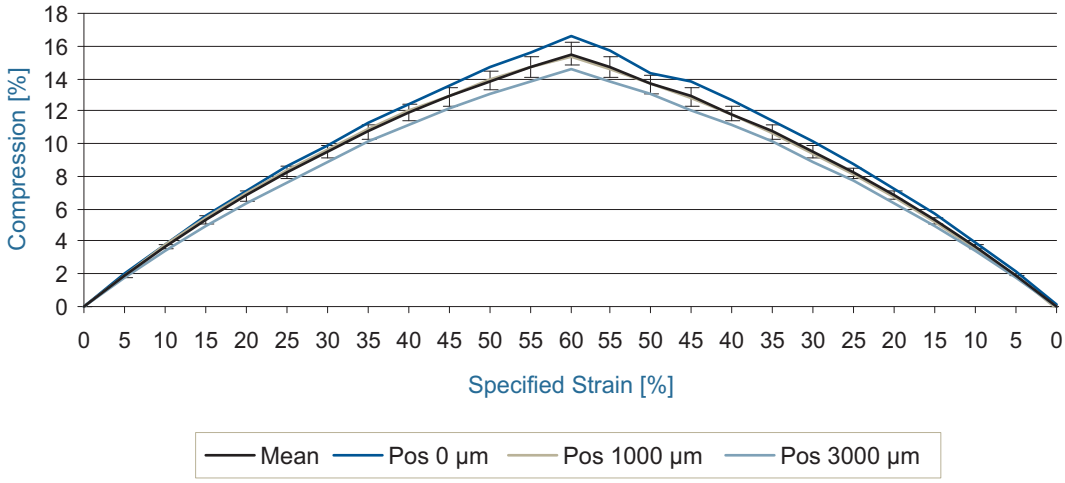

Figure 15 Compression in transversal direction. Similarly to measuring actual strain in axial direction (Fig. 14), compression in transversal direction was determined. At strain amplitudes that were mostly used in the experiments ($20 - 30$ %), compression reaches values of $7 - 10$ %. The curves show, in color, measurements at three different positions and, in black, means of all experiments $\pm$ standard error of mean.

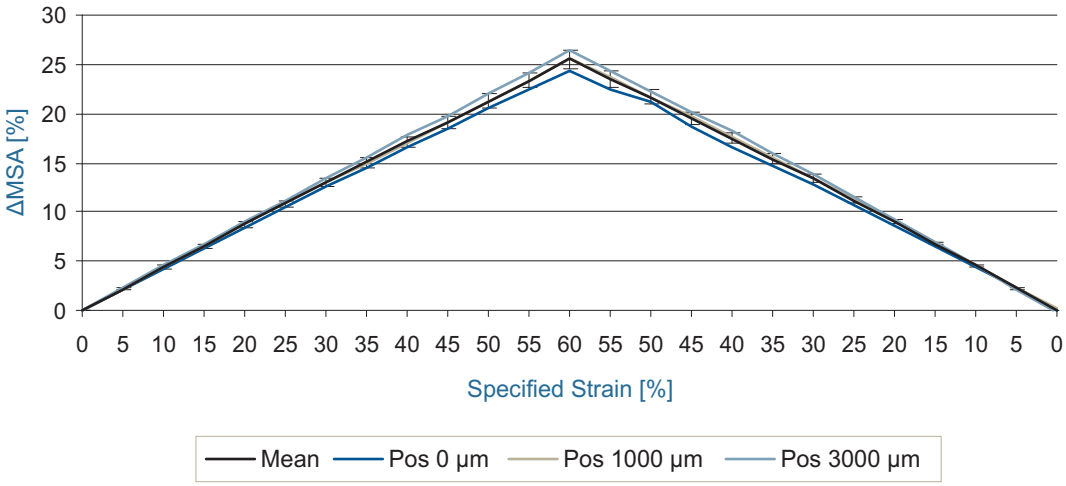

Figure 16 Change in membrane surface area (ΔMSA) depending on specified uniaxial strain. Deriving from actual strain and compression (Figs. 14, 15), the relative increase in MSA was calculated. Actual ΔMSA is at about half of the specified strain because of transversal compression. The curves show, in color, measurements at three different positions and, in black, means of all experiments ± standard error of mean.

3.1.4 Effectiveness of Motion Compensation

A sample image series showing the effectiveness of motion compensation is presented in figure 17.

For the motion compensation mechanism to work properly, the whole setup—strain device and microscope stage—had to be calibrated as explained in section 2.1.3 and tested in section 3.1.1. Once done, the perceived movement of the field of view of the microscope was measured several times ($n = 5$) at different positions under increasing strain. Results were pooled and are shown in figure 18. As can be seen in the graph, the displacement of the field of view increases linearly with applied strain and decreases again in the same way under relaxation hinting at a systematic error. The absolute displacement assumes values of 3.7 % ± 1.2 % (mean ± SEM) at 50 % strain meaning that, for example, when the membrane is observed at position 2000 μm and stretched by 50 % the field of view is shifted by approximately 74 μm—and accordingly by 111 μm at position 3000 μm.

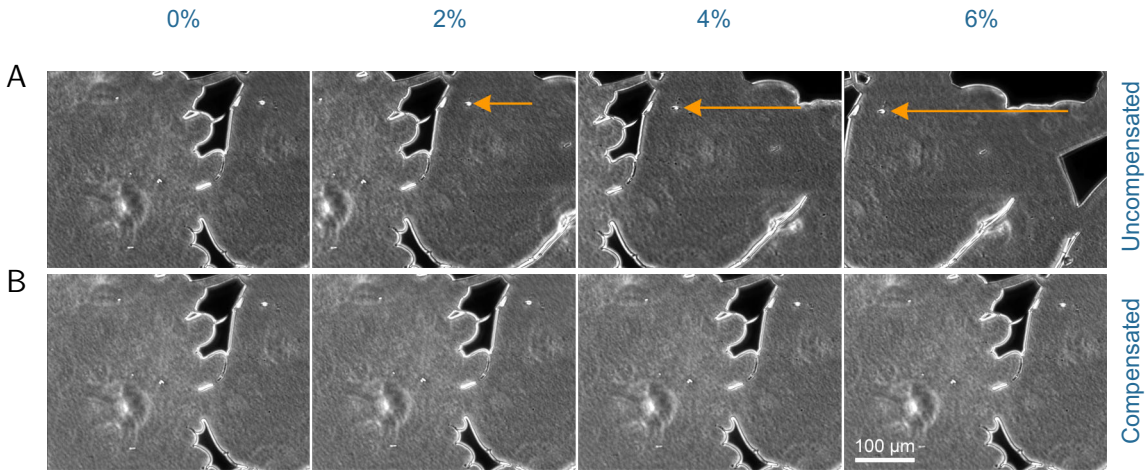

Figure 17 Example of motion compensation. A membrane stained with ink and moved 2950 μm away from the center was incrementally stretched (labels in first row) and images were acquired for each step. A illustrates how the initially observed area moves out of the field of view in the left direction. Using the motion compensation mechanism, this distracting effect can be avoided and the field of view remains almost constant (B). The labels on top indicate the amount of strain at which the images below have been acquired.

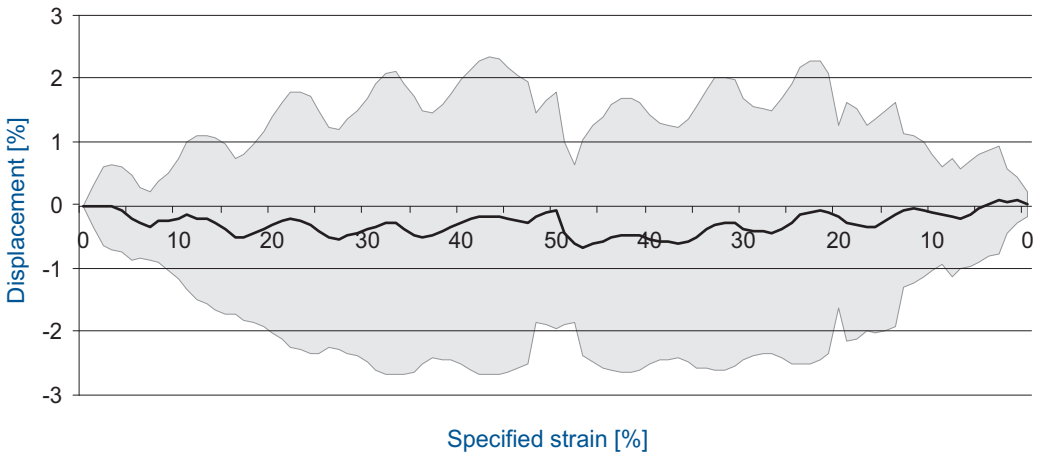

Figure 18 Displacement of field of view when applying strain using motion compensation. A number of tests were performed (at positions between 2000 μm and 3575 μm, $n = 5$) where a stained membrane was stretched up to 50 %, then going back to the relaxed state using the software-controlled motion compensation mechanism acquiring images at each step. Afterwards, features in the images were manually tracked to determine the displacement of the field of view. The absolute offsets were expressed as percentaged error values by relating them to the starting position. Values are shown as means ± standard error of mean.

3.2 Manual vs. Automated Detection of Calcium Peaks

Before using the automated method for detection of transient calcium peaks, it was compared to the results from manual analysis to show that it is a reliable alternative (Fig. 19). Evaluating a data set with 101 cells from 10 experiments from the increasing amplitudes protocol, a highly significant correlation between the results of the manual and automated method was ascertained ($p < 0.001$, two tailed t-test) and no relevant difference in absolute calcium peak counts was found ($p = 0.78$, paired t-test), designating the automated method as a valid alternative for detecting calcium peaks.

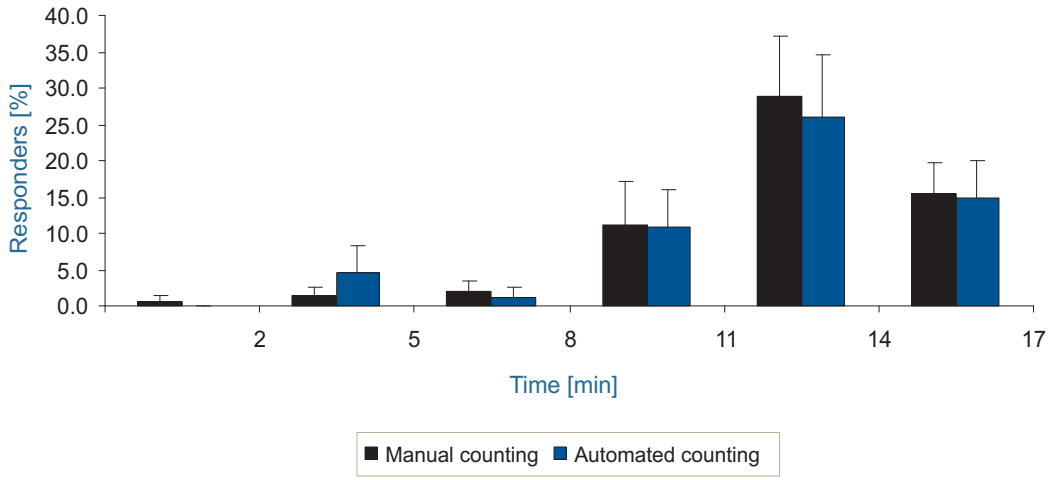

Figure 19 Comparison of manually and automatically detected calcium peaks. The same set of data—in this case the results from the increasing amplitudes strain protocol—was analyzed once manually and once using the automated method described in section 2.6.1. Bars represent mean percentage of cells showing calcium peaks (plus standard error of mean).

3.3 Investigations on Alveolar Type II Cells

Table 12 gives an overview of the experiments and some of their results listing number of experiments, analyzed cells, and responding cells for both LB fusions (FM1-43 fluorescence) and transient calcium peaks (Fura-2 fluorescence). Although most experiments were conducted using dual fluorescence measurements, this was not true for all and, therefore, the numbers for experiment and cell counts differ for both detection methods. When using first generation membranes (see Fig. 5A) only FM1-43 fluorescence was deployed, since it is not reasonable to measure Fura-2 fluorescence due

to increased membrane thickness and higher background illumination, which impedes analysis.

Table 12 General overview of strain protocols. "Cell count" refers to the number of cells that were included in the statistics, excluding cells that showed signs of cell damage (cf. section 3.3.3). (LB = lamellar body)

	FM1-43			Fura-2		
Protocol	**Number of experiments**	**Cell count**	**Cells with LB fusions**	**Number of experiments**	**Cell count**	**Cells with calcium peaks**
Control	12	145	2 (1.4 %)	7	65	0 (0.0 %)
20 % cyclic strain, 2 min pause	15	197	23 (11.7 %)	6	48	6 (12.5 %)
30 % cyclic strain, 2 min pause	8	127	9 (7.1 %)	8	125	10 (8.0 %)
20 % cyclic strain, 30 s pause	12	137	13 (9.5 %)	5	68	4 (5.9 %)
30 % cyclic strain, 30 s pause	11	121	5 (4.1 %)	11	121	9 (7.4 %)
2 Hz cyclic strain, 30 s pause	15	178	10 (5.6 %)	6	56	3 (5.4 %)
Increasing amplitudes	18	211	18 (8.5 %)	13	101	31 (30.7 %)

3.3.1 Mechanical Strain Induces Lamellar Body Fusions

Most of the over 100 experiments were conducted using FM1-43 fluorescence—many times in combination with other dyes—in order to investigate LB fusions (Fig. 20). Figure 21 illustrates the relative number of cells that exhibited LB fusions during the experiments and compares the individual strain protocols. Using one-way ANOVA, no significant difference between the strain protocols was found, most probably due to the high variance of fusion events. However, pairwise comparison with control, where no strain was applied, indicates that all strain protocols increased the rate of fusion events—with a significant difference for the 20 % cyclic strain with 2 min pauses protocol ($p < 0.01$, two tailed, unpaired t-test) and the increasing amplitudes protocol ($p = 0.02$).

When looking at the increasing amplitudes protocol in more detail, it is interesting to note that strain amplitude influences the number of responding cells ("responders"), i.e. the number cells exhibiting LB fusions (see Fig. 22). The number of responders increases with strain amplitude, starting at an amplitude of 25 %, reaching a peak at 30 % ($p < 0.05$, compared to zero and 20 % strain, one-way ANOVA), and dropping

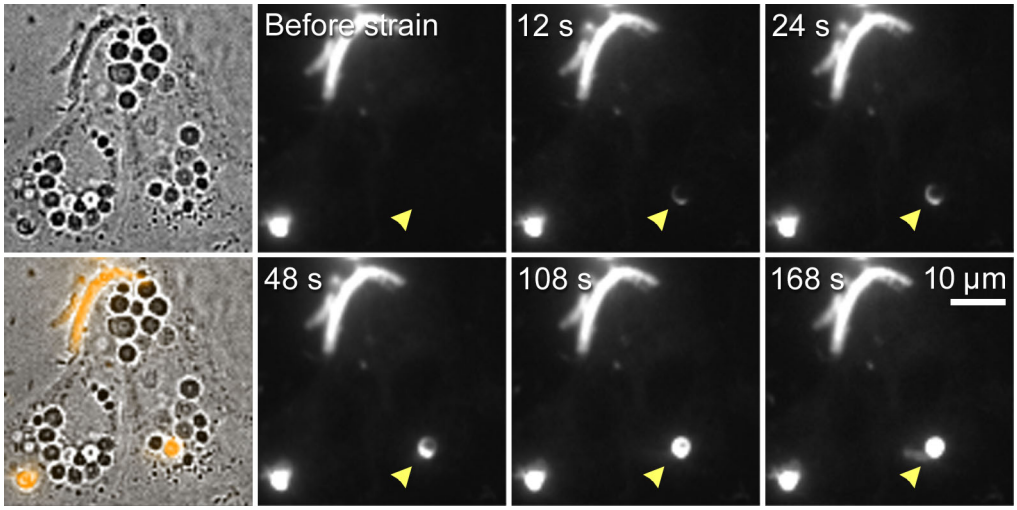

Figure 20 Example of lamellar body fusion taken from a sequence of the increasing amplitudes protocol. The first column shows two cells—once, the original bright field image and once, an overlay of the bright field image with FM1-43 fluorescence (168 s after strain). The other images are taken from a time-lapse series and show FM1-43 fluorescence over time. At 0 s a 30 % strain pulse was applied, and as a result a lamellar body in the alveolar type two cell to the right fused (arrow), even presenting a stick-like extension that can be seen sometimes.

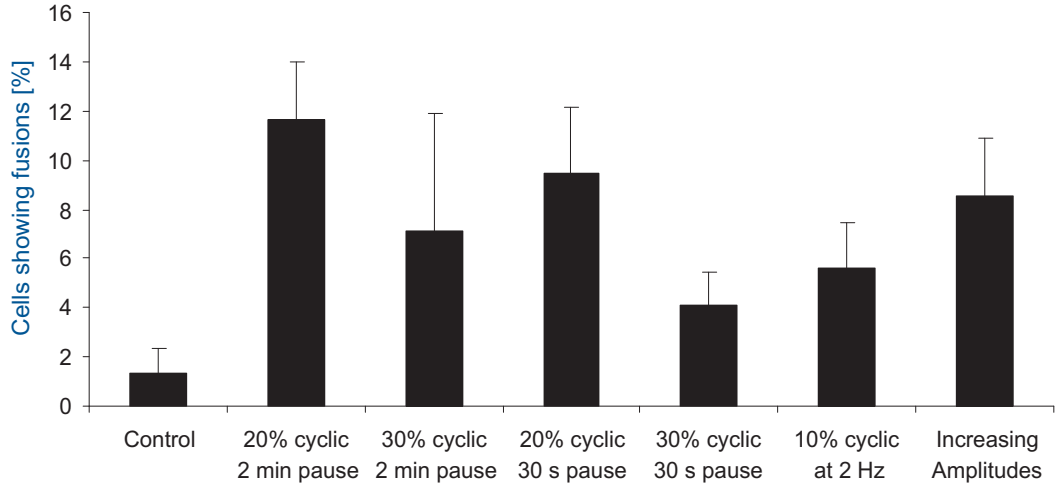

Figure 21 Vesicle fusions detected with FM1-43, comparing different strain protocols. Although the 20 % cyclic strain with 2 min pauses protocol (as well as the other strain protocols) showed a higher number of lamellar body fusions than control, this difference was not statistically significant (one-way analysis of variance). The bars show mean percentage of cells exhibiting lamellar body fusions (plus standard error of mean).

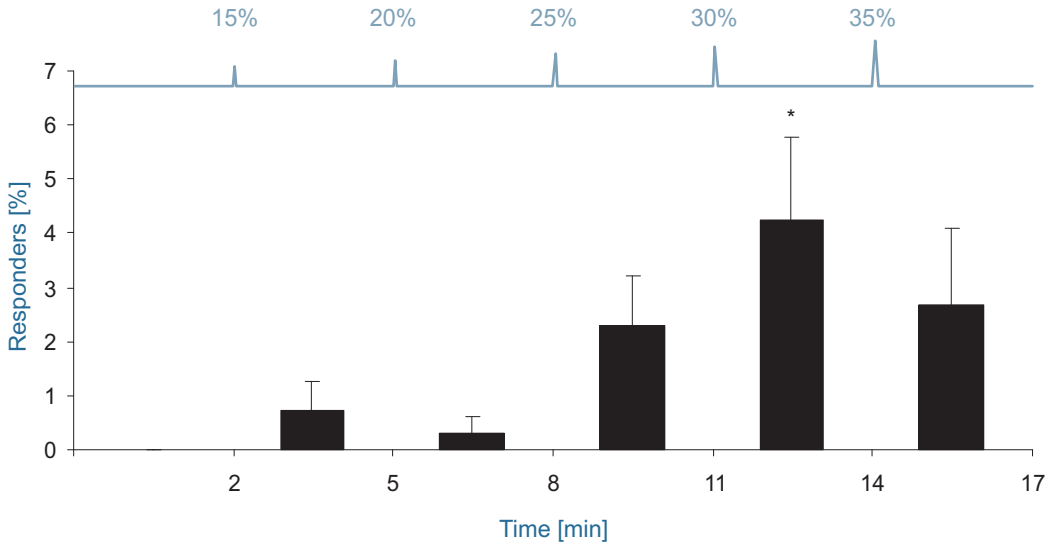

Figure 22 Lamellar body fusions over time shown for the increasing amplitudes protocol. Fusions events were grouped by cycle. The chart shows the applied strain per cycle additionally to the time scale. After 30 % strain, significantly more lamellar body (LB) fusions were seen than at zero and 20 % strain ($p < 0.05$, one-way analysis of variance). Bars represent mean percentage of cells exhibiting LB fusions (plus standard error of mean).

again at higher strain amplitudes. It is important to note, however, that the cells were not directly exposed to a specific strain amplitude, but were exposed to strain pulses again and again in succession.

3.3.2 Calcium Measurements

Using two fluorescent dyes, FM1-43 and Fura-2, many experiments were conducted with the intent to detect both LB fusions and transient increases in intracellular calcium concentration ($[Ca^{2+}]_i$). For analysis the automated method for detecting these calcium peaks was used (cf. section 2.6.1 and 3.2). Figure 23 shows an example of a group of AT II cells responding to strain by a transient elevation of $[Ca^{2+}]_i$.

Figure 24 gives an overview of transient $[Ca^{2+}]_i$ peaks for all strain protocols. Highest number of responding cells (30.7 % ± 9.5 %, mean ± SEM) was seen with the increasing amplitudes protocol, even more than with all other tested protocols. Still, compared to control that showed no transient calcium peaks, it is obvious that the application of strain, in any of the tested ways, induced an intracellular calcium increase.

Having a closer look at the increasing amplitudes protocol (Fig. 25), the distribution of the number of calcium responders looks very similar to the number of cells showing LB fusions (cf. Fig. 22). In fact, there is a highly significant correlation between the

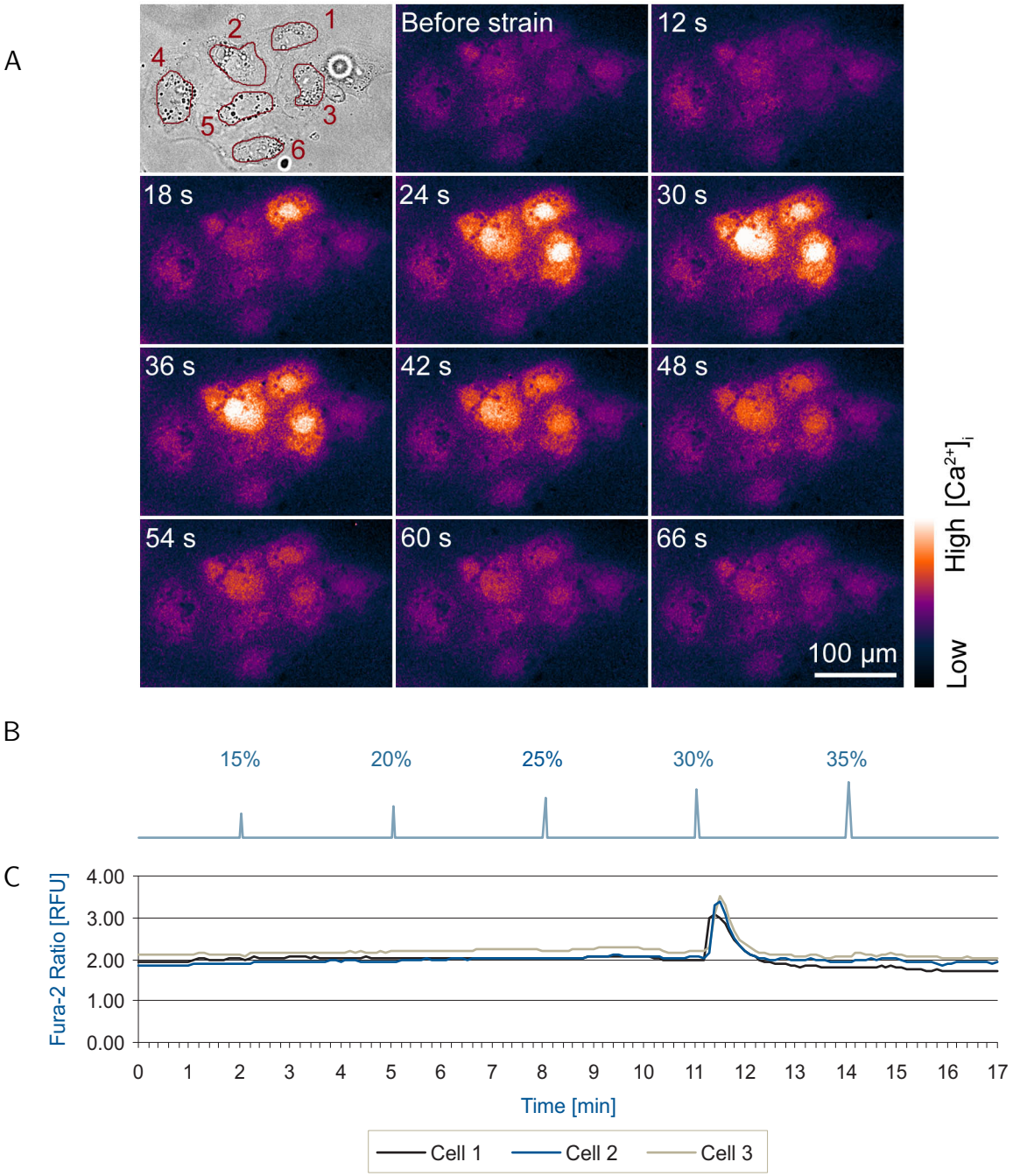

Figure 23 Example of transient calcium peaks taken from a sequence of the increasing amplitudes protocol. A: The top-left, brightfield image depicts the outlines of six cells, which were used for determining mean Fura-2 ratios. The other images show a time-lapse sequence of these ratios in false colors, whereas the first one is immediately before the 30 % strain pulse and the second one (12 s) the first focused image directly after it. B shows the strain protocol over time, and C illustrates the course of intracellular calcium concentration ($[Ca^{2+}]_i$) of three responding cells (see top-left image in A) with a peak after 30 % strain, corresponding to the image sequence in A. (RFU = relative fluorescence units)

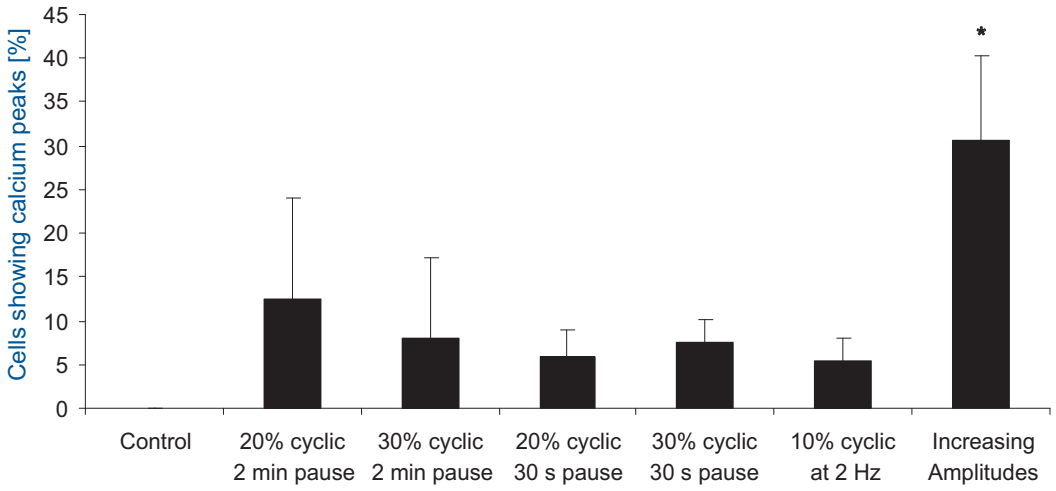

Figure 24 Transient calcium peaks detected with Fura-2. The increasing amplitudes protocol elicited significantly more transient calcium peaks than unstretched control ($p < 0.05$, one-way analysis of variance). Bars represent mean percentage of cells showing transient calcium peaks (plus standard error of mean).

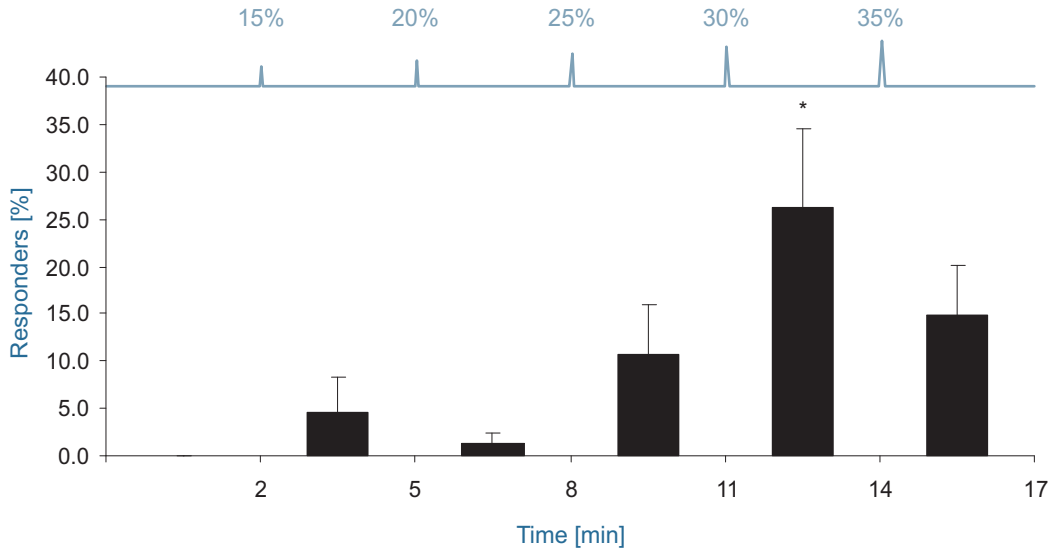

Figure 25 Transient calcium peaks over time shown for the increasing amplitudes protocol. Calcium events were automatically detected as described in section 2.6.1 and grouped by cycle. The chart shows the applied strain per cycle additionally to the time scale. After application of 30 % strain, significantly more calcium peaks were seen than at unstretched control and after 15 % and 20 % strain ($p < 0.05$, one-way analysis of variance). Bars represent mean percentage of cells showing transient calcium peaks (plus standard error of mean).

fraction of calcium responders and the fraction of fusion responders ($p < 0.001$, two tailed t-test). The number of responders increases with strain amplitude, reaching a maximum at 30 % strain and decreasing again at higher strain amplitudes.

When conducting dual fluorescence measurements (FM1-43 and Fura-2), sometimes a transient increase of $[Ca^{2+}]_i$ coincided with a LB fusion, as captured by the image sequence in figure 26. Immediately following a strain pulse, one of the depicted AT II cells responded with an elevation of $[Ca^{2+}]_i$ and, simultaneously, one of its LBs fused (Figs. 26, 20). Unfortunately, the time resolution used for image acquisition in the experiment (6 s) was too coarse to determine which event occurred first–the rise of calcium or the fusion.

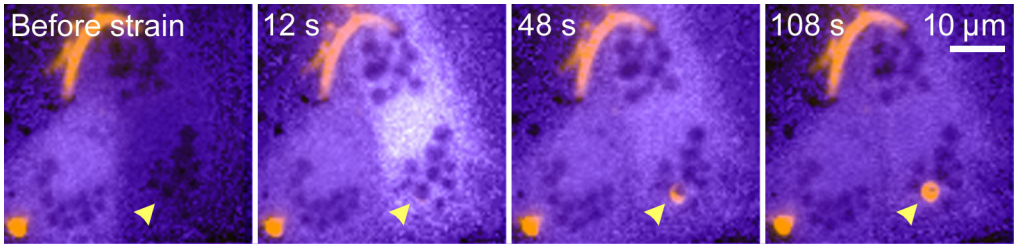

Figure 26 Overlay of FM1-43 (orange) and Fura-2 fluorescence (purple). The first image depicts the situation immediately before application of 30 % strain, whereas the other images show the state after the pulse. Two cells are depicted; the left one already has an elevated intracellular calcium concentration ($[Ca^{2+}]_i$) and does not respond to the applied strain. In the cell to the right, however, $[Ca^{2+}]_i$ increases noticeably for a short time (second image) and subsides again in the following 90 s (third and forth image). At the same time as $[Ca^{2+}]_i$ increases, a lamellar body fuses (arrow). The images were taken from an experiment with the increasing amplitudes protocol (Fig. 20).

3.3.3 Cells Show Damage Under Increasing Strain

Sometimes during experiments single cells showed a dramatic increase in FM1-43 fluorescence and, simultaneously, a drop in Fura-2 fluorescence—at both wavelengths and also in the ratio. Cells exhibiting this behavior were considered damaged and excluded from regular analysis, instead recording these events separately for further investigation. Figure 27 illustrates the relative amount of damaged cells for the increasing amplitudes protocol, for which this phenomenon was investigated and documented best.

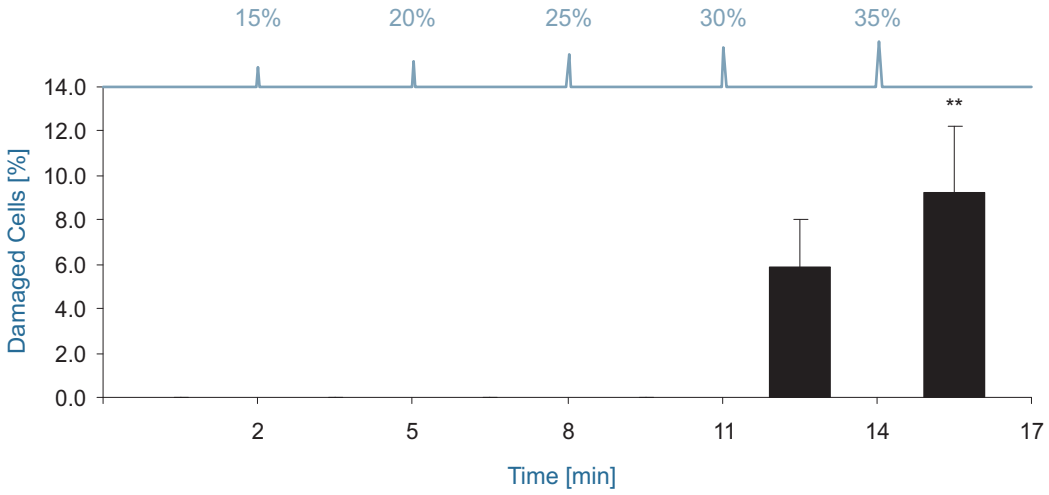

Figure 27 Cell damage for increasing amplitudes protocol. After 11 min and, more prominently, after 14 min, i.e. after applying a strain pulse of 30 % and 35 % respectively, cells started to show signs of damage—an elevation of FM1-43 fluorescence and loss of Fura-2 fluorescence. Compared to the first two minutes of the protocol, where no strain was applied, and to cycles with a lower strain amplitude, this is a significant difference (**: $p < 0.01$, one-way analysis of variance). Bars represent mean percentage of cells showing signs of damage (plus standard error of mean).

Chapter 4

Discussion

4.1 Methodological Aspects of Cell Strain

Since most existing cell-stretching devices are limited by a movement of the sample along the strain axis out of the narrow field of view, in this study a new method for investigating living cells under uniaxial strain or compression was established that allows to keep a region of interest in the field of view of the microscope by utilizing a motorized stage controlled by a motion compensation mechanism (Gerstmair et al.). The major improvement of this method is that single cells under high optical magnification and spatial resolution can be imaged during strain or compression without the need for a cell to be located in the center of the strain field to prevent optical displacement. This removes the main uncertainty from the experiment, which has yet been a major obstacle for studying acute morphological and functional adaptations of a living cell to uniaxial strain.

4.1.1 Device Characteristics

The tests of the strain device revealed that it works reliably and is straightforward to handle. Calibration and setup of the device took only a few minutes and, once done, membrane chambers could be easily attached to and detached from the device allowing to run many experiments in succession. The strain device has some weaknesses, though, in absolute positioning of the stage and application of the right amount of strain. The errors, however, are systematic and can be eliminated or at least reduced by adjusting device parameters and mechanics.

Although stage movement and absolute positioning deviated by about 3 % from the

specified position (see section 3.1.2), this did not affect live cell imaging. Standard procedure was to look for an area with suitable cells by moving the stage around appropriately and to arrest this position during application of strain by compensating outwards directed motion. Absolute positioning was rarely necessary and moving backwards and forwards between two points was repeatable.

Measuring actual amount of uniaxial strain in several experiments showed that the membranes actually were stretched less than specified, for example, 25 % instead of 30 %. The error increases almost linearly with the specified amount of strain (Fig. 14) suggesting the error is systematic and can probably be reduced by adjusting the internal parameters of the software that controls the warp component of the strain device. There is, however, a non-linear component that adds up to the error of actual membrane strain that may be explained by the retraction force of the membrane that increases with applied strain.

Because of inherent material properties elastic membranes contract in transversal direction (perpendicularly to the applied strain). For example, for the membranes used in the experiments this contraction amounted to roughly 10 % at 30 % stretch and was dependent on the distance to the center of the membrane with most contraction at the center itself and less contraction in the periphery (Fig. 15). However, the effect of membrane position on compression was negligible for regular experiments (9.9 % at the center vs. 8.9 % at a distance of 3000 μm at 30 % strain). As can be seen in the graph, at higher strain levels the effects of contraction decrease resulting in a more linear deformation of the membrane. This fact can be exploited by growing cells on membranes with a high prestrain (most of the time we used a prestrain of 40 %). Membrane contraction in perpendicular direction, however, is a common problem in uniaxial cell stretching and, up until now, only few approaches were developed to counteract the effect, for example, Pfister et al. (2003) designed a special elastic membrane chamber with a small well and thick walls and Waters et al. (2001) used a cruciform membrane clamped at each side. In the end the question remains how different kinds of strain affect cells and their behavior and in which way a small contraction in perpendicular direction affects the response to a uniaxially applied strain.

Resulting from measurements of actual strain in axial and transversal direction, changes in membrane surface area (ΔMSA) were determined (Fig. 16). Unlike the individual directional components, i.e. axial strain and transversal contraction, the MSA depended strictly linearly on specified uniaxial strain. As previously described, due to transversal contraction absolute values of ΔMSA were less than the specified values

for a pure uniaxial deformation. AT II cells attached well to the elastic membranes after 24 h incubation and did not lose contact during the experiments (at strain levels of up to 35 %), as verified in random samples by comparing the outlines of cells after stretch and relaxation with the original outlines before stretch. This is also consistent with other studies using AT II cells grown on silicone membranes (Tschumperlin and Margulies, 1998; Frick et al., 2004).

4.1.2 Motion Compensation

With the motorized strain device and custom-written software we established a new method for stabilizing the field of view when investigating cells under uniaxial strain using fluorescence or brightfield microscopy. Motion compensation allows to design strain protocols that are otherwise difficult, if not impossible to implement, like applying and keeping strain at a specific level for some time or observing cells during stretch. Although it is possible to manually follow an observed area that is moving out of the field of view, this takes time and may not be fast enough for high strain rates or levels. Furthermore, where previously one was restricted in the selection of a region of interest on an elastic membrane to the center that is not subject to outwards directed movement during stretching, the compensation mechanism allows to choose almost any region on the membrane and observe the effects of strain on cells.

Evaluation of the motion compensation mechanism (Fig. 18) revealed that even for higher strain levels (up to 50 %) and positions up to several millimeters away from the center of the membrane the originally observed area was kept in the field of view. In the worst case the area 3000 μm away from the center would move by 60 μm at 50 % stretch, which is still covered by the field of view of the microscope (450 μm $\times$ 340 μm) when using a 40$\times$ objective. In some experiments positions of up to 6000 μm away from the center were selected for investigation without causing any difficulties during image acquisition and analysis. However, even when using motion compensation there is a small displacement of the observed area and it increases almost linearly with applied strain, which is mainly attributed to the error in axial strain (Fig. 14). Since the compensation mechanism calculates the new position of an observed area from its previous position and the applied strain, an incorrect previous position or an error in the actual strain results in an inaccurate motion compensation. Hence, the correction of actually applied strain should further improve the accuracy of motion compensation.

For the implementation of the motion compensation mechanism an open loop control relying solely on the position of the membrane and, therefore, a precise calibration was

chosen. Another approach would be to implement a closed loop control by adding visual feedback and movement correction via a digital camera and computer vision algorithms. Visual feedback, however, might be difficult to acquire because either the light path of the microscope would have to be split or the camera images shared by two applications. Additionally, the image processing could interfere with and slow down the acquisition of time-lapse series or increase bleaching effects when using fluorescence microscopy. Since the closed loop approach works very efficiently, there is no need to change the current implementation.

4.1.3 Membrane Behavior Under Strain

As has been previously described by others (Frick et al., 2004; Brown, 2000) when stretching (or compressing) a membrane under live cell imaging conditions another aspect becomes important: the thickness of the membrane—and therefore the focal plane—changes making an adjustment of the microscope focus necessary. Although changes in membrane thickness were small (in the sub-micrometer range), they became relevant when using high magnification (40× objective) or oil immersion. Hence, in this study short strain pulses were applied and images were always acquired at zero strain during pauses in the strain protocol. In ongoing experiments we are using strain protocols with plateaus or with low strain rates and are manually adjusting the microscope focus. Of course, another approach would be to use an objective with a different depth of focus.

We also found that after application of a strain pulse the membrane needed a short time (up to 3 s) to settle down and reach a stable state, especially when using the oil immersion. Images acquired during this phase were often out of focus and, therefore, discarded. Depending on strain rate and level this hysteresis behavior can limit the time resolution of image acquisition.

4.2 Investigations on Alveolar Type II Cells

4.2.1 Lamellar Body Fusions After Mechanical Stimulation

LB fusions and, therefore, surfactant secretion can be stimulated by mechanically stretching AT II cells as has been previously shown in other studies (Wirtz and Dobbs, 1990; Ashino et al., 2000; Frick et al., 2004). Applying different strain protocols—slow and fast cyclic protocols and one with increasing amplitudes—this was confirmed

(Fig. 21), however, no significant difference was found between the various stimuli. The randomness and small number of stimulated fusion events in single type II cells is a general problem which hampers statistical analysis. This applies particularly to unpaired experiments from different animals and lung tissues and is reflected in the high standard deviations in figure 21. Consequently, there is no clear distinction between the tested protocols in inducing LB fusions, however, the following protocols showed response rates in the range of 8 % to 12 % and seem to be suitable for further experiments: 20 % cyclic strain with 2 min pause, 20 % cyclic strain with 30 s pause, and increasing amplitudes with 3 min pause.

The increasing amplitudes protocol showed an interesting finding: the number of fusion responders increased with strain level up to 30 %, however, it decreased again at the highest strain amplitude (35 %). This circumstance needs to be further examined, for example, by reversing the order and using a decreasing amplitudes protocol, because it could be that, using the increasing amplitudes protocol, the cells already responded at a lower strain amplitude and are in an inactivated state. Wirtz and Dobbs (1990) also found a similar correlation between the magnitude of stretch and the magnitude of secretion with a significant increase in secretion starting at a change of cell surface area (CSA) of +16 % corresponding to roughly +35 % nominal uniaxial strain with the strain device used in this study (Fig. 16). Accordingly, in a study by Frick et al. (2004) AT II cells started to respond with fusions at a strain amplitude of 20 % increase in CSA reaching higher response rates at higher strain amplitudes (with a maximum at 40 % increase in CSA). The amounts of strain used in our study correspond well with reported changes of the alveolar cell membrane basement membrane area in vivo (Tschumperlin and Margulies, 1999).

4.2.2 Automated Detection of Transient Calcium Peaks

For analyzing the high number of experiments with calcium imaging we resorted to a semi-automated approach that calculated the Fura-2 ratio and used its course over time (and its derivatives, see section 2.6.1) to classify if a cell responded, i.e. showed a transient rise in $[Ca^{2+}]_i$. Thus, instead of evaluating the Fura-2 ratio for every single cell manually, the semi-automated approach proved to be fast and—most importantly—unbiased. The results of the semi-automated and manual approach were comparable and showed no significant difference. A drawback of the used approach is that it does not detect calcium peaks with slowly increasing $[Ca^{2+}]_i$ (an increase that takes more than 18 s). This kind of calcium peak, however, occurred infrequently and can most

probably be attributed to a different cellular mechanism (Knot et al., 2005).

4.2.3 Transient Calcium Peaks Depend On Strain Protocol and Amplitude

Along with FM1-43 fluorescence for tracking LB fusions Fura-2 fluorescence was used in many experiments to measure $[Ca^{2+}]_i$. As Wirtz and Dobbs (1990) and others (Haller et al., 1999; Ashino et al., 2000; Frick et al., 2004) have shown, rises in $[Ca^{2+}]_i$ are involved in exocytosis of surfactant by AT II cells and, actually, precede LB fusions. Preliminary to further experiments designed to elucidate the role of $[Ca^{2+}]_i$ in cellular mechanotransduction and details of the associated signaling cascade we investigated which strain protocol—and hence which respiration pattern—might result in a high number of AT II cells responding with transient rises in $[Ca^{2+}]_i$. This may have clinical implications to select the optimal respiration depth and frequency in diseased, mechanically ventilated patients with low compliance. Testing six different strain protocols and a series of control experiments, where no strain was applied, interestingly no significant difference was found between the cyclic protocols (Fig. 24), whereas the increasing amplitudes protocol resulted in significantly more cells responding with a transient $[Ca^{2+}]_i$ rise. This finding suggests that the total number of strain pulses, i.e. very short phases of cell stretch and relaxation, is less important for evoking $[Ca^{2+}]_i$ peaks than their amplitude and sequence and it could be that lower strain pulses cause a state of pre-excitation of the cells that facilitates calcium signaling on subsequent stimuli. Future experiments using high initial strain amplitudes of decreasing magnitude will help to gain more insight into these questions.

In order to determine how the strain amplitude affected the number of cells responding with a transient $[Ca^{2+}]_i$ rise ("calcium responders"), the increasing amplitudes protocol was tested (see section 2.7 and Fig. 25). It was found that similar amounts of uniaxial strain were necessary to elicit calcium peaks as in a previous study by Frick et al. (2004) using equibiaxial strain: 25 % to 30 % uniaxial strain (20 % to 25 % actual strain, Fig. 14) vs. 20 % equibiaxial strain. However, when considering transversal compression of the membrane on applying uniaxial strain, the actual MSA changes were less for the uniaxial strain (10 % to 13 %, Fig. 16).

When comparing "calcium responses" with LB fusion events in dual fluorescence (FM1-43 and Fura-2) experiments, we found a highly significant correlation (Figs. 22 and 25) that reinforces the concept of calcium signaling being necessary for surfactant secretion (Frick et al., 2001, 2004). Although the number of cells responding with a transient calcium peak depends on the same way on the strain amplitude as the

number of cells responding with LB fusions, there is still a difference in the relative number of responses with roughly six times more calcium responses than LB fusion events. Obviously, not every strain pulse leads to a transient calcium rise and not every transient calcium rise leads to a LB fusion, which stresses the point that there are many factors influencing cellular mechanotransduction (Liu et al., 1999b; Vlahakis and Hubmayr, 2003).

4.2.4 Detecting Membrane Damage With FM1-43 and Fura-2

Mechanical strain not only has physiological effects on AT II cells but also pathophysiological ones like membrane damage when the structure of a cell changes too fast or when the deformation is too high (Tschumperlin and Margulies, 1998; Tschumperlin et al., 2000; Vlahakis and Hubmayr, 2000; Hammerschmidt et al., 2004; Felder et al., 2008). In our experiments—particularly when applying the increasing amplitudes protocol—we could observe the phenomenon that single cells showed an increase in FM1-43 and a synchronous decrease in Fura-2, probably caused by a damaged membrane that allowed, on the one hand, the cell impermeant dye FM1-43 to enter the cytoplasm and stain intracellular membranes and, on the other hand, the intracellular Fura-2 to leak out of the cells. Membrane damage was observed starting at 30 % uniaxial strain (+13 % MSA) and increased, as expected, with 35 % strain (Fig. 27), being consistent with the results of Tschumperlin and Margulies (1998). Future tests employing fluorescent dyes like Ethidium Homodimer-1 and Calcein AM (as in Tschumperlin and Margulies, 1998) will be necessary to test if the observed changes in FM1-43 and Fura-2 fluorescence are an effective marker of damage in AT II cells.

4.3 Future Directions

4.3.1 Improvements on the Strain Device

In order to improve the accuracy of stage movement, a gear with a high reduction (246:1) was attached to the stage motor. Since very high precision (in the submicrometer range) is not required and the high reduction decreases acceleration and maximum speed of the stage, the gear will be replaced by one with a lower reduction (e.g. 20:1), which will also allow higher strain rates when using motion compensation at areas far away from the membrane center.

Since the elastic membranes change in thickness under strain and the microscope focus has to be adjusted accordingly, it would be very helpful to have a compensation mechanism that considers the current strain level and automatically adjusts the focus. Although the mechanism itself should be rather straightforward to implement since there is a similar correlation between strain level and membrane thickness as with strain level and transversal contraction, there are technical constraints that make it difficult, like access to the motorized focus drive, which is controlled by the microscope stage control and image acquisition software.

4.3.2 Investigations on AT II Cells

Increasing Time Resolution of Image Acquisition. For calcium measurements the ratiometric dye Fura-2 AM was used, most of the time along with FM1-43 for detecting LB fusions, requiring images to be acquired at two different wavelengths (or three if FM1-43 was included) at each time point. Considering filter switching, shutter, and exposure times, this resulted in a maximum rate of about two frames per second, which is not fast enough for visualizing different entities of intracellular calcium signaling that may have a duration of less than 300 ms (Knot et al., 2005). Therefore, a method for high-resolution calcium imaging suggested by Leybaert et al. (1998) could be employed, where images are acquired continuously at the first wavelength and intermittently at the second wavelength, thus reducing acquisition time but still adjusting for bleaching and changes in dye concentration. Alternatively, a different, non-ratiometric fluorescent dye like Fluo-4 could be used (Gee et al., 2000), however, in preliminary tests its handling and the loading of cells proved to be more difficult than with Fura-2 AM.

The Role of TRP Channels. Currently, it is not clear which mechanism causes the $[Ca^{2+}]_i$ rises in AT II cells in response to uniaxial or equibiaxial mechanical strain, however, members of the TRPC and TRPV family—mechanosensitive ion channels—have been proposed as potential candidates since they are expressed in lung cells and can be activated by mechanical forces (Nilius et al., 2004; O'Neil and Heller, 2005; Hamanaka et al., 2007). Hence, the next step in the investigation of calcium signaling in AT II cells is to test the effect of inhibitors and activators of TRP ion channels on transient calcium peaks and, possibly, LB fusion events.

Cell Compression. Because most existing studies have concentrated on tensile cell strain, information on compression of epithelial or endothelial cells, such as during alve-

olar collapse, bronchoconstriction, or vasoconstriction is sparse (Ressler et al., 2000). When growing cells on a prestretched membrane, however, the strain device would allow to investigate the effects of cell compression by relaxation of the membrane in a defined manner resulting in a contraction of the attached cells. Such compression protocols may shed more light on the way mechanical forces affect intra- and intercellular structures and cellular behavior.

4.4 Conclusions

The major improvement of the method described here is that single cells under high optical magnification and spatial resolution can be imaged during strain or compression without the need for a cell to be located in the center of the strain field to prevent optical displacement. Motion compensation makes new experimental protocols possible and simplifies working with the strain device. Although the current prototype of the strain device has some minor systematic errors concerning stage movement and applied strain and needs to be fine-tuned, it already passed a series of real-world experiments with dual fluorescence microscopy and works efficiently enough to investigate cellular changes under dynamic conditions (Gerstmair et al.). Further improvements include support frames that can be adjusted to an arbitrary prestrain and inhibit rotations of the membrane holders (of the third generation membrane chambers), thus alleviating the handling of membrane chambers that can be transferred easily from an incubator to the strain device without membrane deformation or movement.

Most important biological applications of the method presented here will be to perform high resolution fluorescence measurements within individual cells or within small groups of cells during strain and/or strain relaxation. Examples using calcium sensitive fluorescent dyes have been demonstrated in this work and a broad spectrum of fluorescent dyes and applications that can be used in live cell imaging and mechanobiology, such as fluorescence resonance energy transfer (FRET) and fluorescence recovery after photobleaching (FRAP), has been recently reviewed in detail (Wang et al., 2008).

Chapter 5

Summary

Mechanical forces play an important role in tissue and cell physiology and influence many aspects of the cell, like behavior, structure, and differentiation, but can also lead to diseases. Because of the biological significance of mechanostimulation and mechanotransduction, many strain-application devices have been developed, most of them custom-made but some also commercially available, with a wide range of modes of operation. When it comes to uniaxial deformations of cells, imaging is usually impeded by movement of the sample along the strain axis out of the narrow field of view. In order to overcome this limitation, we established a new method that keeps a region of interest in the field of view of the microscope by utilizing a motorized stage controlled by a motion compensation mechanism. Given the current position of interest on the specimen and the strain or compression to be applied, the implemented algorithm calculates the expected displacement and, synchronously to applying the deformation, directs the motorized stage to follow accordingly, thus stabilizing the observed area during imaging.

Movement and strain tests showed that the system worked reliably and simplified the handling of specimens, mounting on the microscope, and setup of experimental protocols with the custom-written software. However, due to not yet optimized manufacturing precision and software calibration the developed strain device exhibits systematic errors concerning positioning of the stage (positive deviation) and strain application (negative deviation), which—since known—can be considered during analysis and are to be eliminated in the ongoing development process. Using motion compensation the absolute displacement of the observed area assumed values of 3.7 % ± 1.2 % (mean ± standard error of mean) at 50 % strain, meaning the originally observed area was always kept in the field of view when using a 40× objective and, hence, achieving the

primary goal of this work.

The system was then tested on primarily cultivated alveolar type two (AT II) cells, in which mechanical effects on secretion have been intensively investigated in the past. Using dual fluorescence microscopy (Fura-2 AM and FM1-43) to detect both transient rises of intracellular calcium concentration ($[Ca^{2+}]_i$) and exocytotic secretion of surfactant, i.e. lamellar body (LB) fusions, a series of strain protocols and their effects on AT II cells were examined. The experiments showed similar effects and thresholds for uniaxial strain as previous studies for biaxial strain with regard to transient $[Ca^{2+}]_i$ rises (threshold at 20 % to 25 % uniaxial strain vs. 20 % equibiaxial strain) and LB fusions. Except for transient $[Ca^{2+}]_i$ rises elicited at a significantly higher percentage by a protocol with increasing strain amplitudes there was no statistically relevant difference in the tested strain protocols.

In conclusion, the system presented here, along with its motion compensation mechanism, allows to apply new experimental protocols and simplifies working with the strain device and specimens. Most important biological applications of the method will be to perform high resolution fluorescence measurements within individual cells or within small groups of cells during strain and strain relaxation.

Bibliography

1. Ashino Y, Ying X, Dobbs LG, Bhattacharya J: $[Ca^{2+}]_i$ oscillations regulate type II cell exocytosis in the pulmonary alveolus. *Am J Physiol Lung Cell Mol Physiol* 279: L5–13 (2000)

2. Avery ME, Mead J: Surface properties in relation to atelectasis and hyaline membrane disease. *AMA J Dis Child* 97: 517–523 (1959)

3. Bader DL, Knight MM: Biomechanical analysis of structural deformation in living cells. *Med Biol Eng Comput* 46: 951–963 (2008)

4. Baker S, Matthews I: Lucas-Kanade 20 Years On: A Unifying Framework. *Int J Comput Vision* 56: 221–255 (2004)

5. Bao G, Suresh S: Cell and molecular mechanics of biological materials. *Nat Mater* 2: 715–725 (2003)

6. Betz WJ, Mao F, Smith CB: Imaging exocytosis and endocytosis. *Curr Opin Neurobiol* 6: 365–371 (1996)

7. Bottlang M, Simnacher M, Schmitt H, Brand RA, Claes L: A cell strain system for small homogeneous strain applications. *Biomed Tech (Berl)* 42: 305–309 (1997)

8. Brown TD: Techniques for mechanical stimulation of cells in vitro: a review. *J Biomech* 33: 3–14 (2000)

9. Christensen AP, Corey DP: TRP channels in mechanosensation: direct or indirect activation? *Nat Rev Neurosci* 8: 510–521 (2007)

10. Clapham DE, Runnels LW, Strübing C: The TRP ion channel family. *Nat Rev Neurosci* 2: 387–396 (2001)

11. Clements JA: Lung surfactant: a personal perspective. *Annu Rev Physiol* 59: 1–21 (1997)

12. Dallas SL, Chen Q, Sivakumar P: Dynamics of assembly and reorganization of extracellular matrix proteins. *Curr Top Dev Biol* 75: 1–24 (2006)

13. Dietl P, Frick M, Mair N, Bertocchi C, Haller T: Pulmonary consequences of a deep breath revisited. *Biol Neonate* 85: 299–304 (2004)

14. Dietl P, Haller T: Exocytosis of lung surfactant: from the secretory vesicle to the air-liquid interface. *Annu Rev Physiol* 67: 595–621 (2005)

15. Dobbs LG, Gonzalez R, Williams MC: An improved method for isolating type II cells in high yield and purity. *Am Rev Respir Dis* 134: 141–145 (1986)

16. Engle WA, Committee on Fetus and Newborn: Surfactant-replacement therapy for respiratory distress in the preterm and term neonate. *Pediatrics* 121: 419–432 (2008)

17. Felder E, Siebenbrunner M, Busch T, Fois G, Miklavc P, Walther P, Dietl P: Mechanical strain of alveolar type II cells in culture: changes in the transcellular cytokeratin network and adaptations. *Am J Physiol Lung Cell Mol Physiol* 295: L849–L857 (2008)

18. Frick M, Bertocchi C, Jennings P, Haller T, Mair N, Singer W, Pfaller W, Ritsch-Marte M, Dietl P: Ca^{2+} entry is essential for cell strain-induced lamellar body fusion in isolated rat type II pneumocytes. *Am J Physiol Lung Cell Mol Physiol* 286: L210–L220 (2004)

19. Frick M, Eschertzhuber S, Haller T, Mair N, Dietl P: Secretion in alveolar type II cells at the interface of constitutive and regulated exocytosis. *Am J Respir Cell Mol Biol* 25: 306–315 (2001)

20. Frye SR, Yee A, Eskin SG, Guerra R, Cong X, McIntire LV: cDNA microarray analysis of endothelial cells subjected to cyclic mechanical strain: importance of motion control. *Physiol Genomics* 21: 124–130 (2005)

21. Gee KR, Brown KA, Chen WN, Bishop-Stewart J, Gray D, Johnson I: Chemical and physiological characterization of fluo-4 Ca(2+)-indicator dyes. *Cell Calcium* 27: 97–106 (2000)

22. Gerstmair A, Fois G, Dietl P, Felder E: A device for simultaneous live cell imaging during uni-axial mechanical strain or compression (????). In preparation.

23. Grynkiewicz G, Poenie M, Tsien RY: A new generation of Ca^{2+} indicators with greatly improved fluorescence properties. *J Biol Chem* 260: 3440–3450 (1985)

24. Haller T, Auktor K, Frick M, Mair N, Dietl P: Threshold calcium levels for lamellar body exocytosis in type II pneumocytes. *Am J Physiol* 277: L893–L900 (1999)

25. Haller T, Ortmayr J, Friedrich F, Völkl H, Dietl P: Dynamics of surfactant release in alveolar type II cells. *Proc Natl Acad Sci U S A* 95: 1579–1584 (1998)

26. Hamanaka K, Jian MY, Weber DS, Alvarez DF, Townsley MI, Al-Mehdi AB, King JA, Liedtke W, Parker JC: TRPV4 initiates the acute calcium-dependent permeability increase during ventilator-induced lung injury in isolated mouse lungs. *Am J Physiol Lung Cell Mol Physiol* 293: L923–L932 (2007)

27. Hammerschmidt S, Kuhn H, Grasenack T, Gessner C, Wirtz H: Apoptosis and necrosis induced by cyclic mechanical stretching in alveolar type II cells. *Am J Respir Cell Mol Biol* 30: 396–402 (2004)

28. Hawgood S, Clements JA: Pulmonary surfactant and its apoproteins. *J Clin Invest* 86: 1–6 (1990)

29. Hayakawa K, Tatsumi H, Sokabe M: Actin stress fibers transmit and focus force to activate mechanosensitive channels. *J Cell Sci* 121: 496–503 (2008)

30. Hu S, Chen J, Fabry B, Numaguchi Y, Gouldstone A, Ingber DE, Fredberg JJ, Butler JP, Wang N: Intracellular stress tomography reveals stress focusing and structural anisotropy in cytoskeleton of living cells. *Am J Physiol Cell Physiol* 285: C1082–C1090 (2003)

31. Huang H, Kamm RD, Lee RT: Cell mechanics and mechanotransduction: pathways, probes, and physiology. *Am J Physiol Cell Physiol* 287: C1–11 (2004)

32. Hung CT, Williams JL: A method for inducing equi-biaxial and uniform strains in elastomeric membranes used as cell substrates. *J Biomech* 27: 227–232 (1994)

33. Ingber DE: Tensegrity II. How structural networks influence cellular information processing networks. *J Cell Sci* 116: 1397–1408 (2003)

34. Ingber DE: Cellular mechanotransduction: putting all the pieces together again. *FASEB J* 20: 811–827 (2006)

35. Iwata Y, Katanosaka Y, Arai Y, Komamura K, Miyatake K, Shigekawa M: A novel mechanism of myocyte degeneration involving the Ca2+-permeable growth factor-regulated channel. *J Cell Biol* 161: 957–967 (2003)

36. Jungbauer S, Gao H, Spatz JP, Kemkemer R: Two characteristic regimes in frequency-dependent dynamic reorientation of fibroblasts on cyclically stretched substrates. *Biophys J* 95: 3470–3478 (2008)

37. Knot HJ, Laher I, Sobie EA, Guatimosim S, Gomez-Viquez L, Hartmann H, Song LS, Lederer WJ, Graier WF, Malli R, Frieden M, Petersen OH: Twenty years of calcium imaging: cell physiology to dye for. *Mol Interv* 5: 112–127 (2005)

38. Kubicek JD, Brelsford S, LeDuc PR: Use of Flexible Materials with a Novel Pressure Driven Equibiaxial Cell Stretching Device for Mechanical Stimulation of Single Mammalian Cells. *Mat Res Soc Symp Proc* 773: 13–18 (2003)

39. Lee AA, Delhaas T, Waldman LK, MacKenna DA, Villarreal FJ, McCulloch AD: An equibiaxial strain system for cultured cells. *Am J Physiol* 271: C1400–C1408 (1996)

40. Leybaert L, Sneyd J, Sanderson MJ: A simple method for high temporal resolution calcium imaging with dual excitation dyes. *Biophys J* 75: 2025–2029 (1998)

41. Li K: The image stabilizer plugin for ImageJ. `http://www.cs.cmu.edu/~kangli/code/Image_Stabilizer.html` (2008)

42. Liu M, Montazeri S, Jedlovsky T, Wert RV, Zhang J, Li RK, Yan J: Bio-stretch, a computerized cell strain apparatus for three-dimensional organotypic cultures. *In Vitro Cell Dev Biol Anim* 35: 87–93 (1999a)

43. Liu M, Tanswell AK, Post M: Mechanical force-induced signal transduction in lung cells. *Am J Physiol* 277: L667–L683 (1999b)

44. Lucas BD, Kanade T: An Iterative Image Registration Technique with an Application to Stereo Vision. In: *Proceedings of the 7th International Joint Conference on Artificial Intelligence (IJCAI '81)* (1981), pp. 674–679

45. Mason RJ, Voelker DR: Regulatory mechanisms of surfactant secretion. *Biochim Biophys Acta* 1408: 226–240 (1998)

46. Mazia D, Schatten G, Sale W: Adhesion of cells to surfaces coated with polylysine. Applications to electron microscopy. *J Cell Biol* 66: 198–200 (1975)

47. Meyers JR, MacDonald RB, Duggan A, Lenzi D, Standaert DG, Corwin JT, Corey DP: Lighting up the senses: FM1-43 loading of sensory cells through nonselective ion channels. *J Neurosci* 23: 4054–4065 (2003)

48. Naruse K, Yamada T, Sokabe M: Involvement of SA channels in orienting response of cultured endothelial cells to cyclic stretch. *Am J Physiol* 274: H1532–H1538 (1998)

49. Nilius B, Vriens J, Prenen J, Droogmans G, Voets T: TRPV4 calcium entry channel: a paradigm for gating diversity. *Am J Physiol Cell Physiol* 286: C195–C205 (2004)

50. O'Neil RG, Heller S: The mechanosensitive nature of TRPV channels. *Pflugers Arch* 451: 193–203 (2005)

51. Pfister BJ, Weihs TP, Betenbaugh M, Bao G: An in vitro uniaxial stretch model for axonal injury. *Ann Biomed Eng* 31: 589–598 (2003)

52. Rasband W: ImageJ - Image Processing and Analysis in Java. `http://rsb.info.nih.gov/ij/index.html` (2008)

53. Ressler B, Lee RT, Randell SH, Drazen JM, Kamm RD: Molecular responses of rat tracheal epithelial cells to transmembrane pressure. *Am J Physiol Lung Cell Mol Physiol* 278: L1264–L1272 (2000)

54. Roe MW, Lemasters JJ, Herman B: Assessment of Fura-2 for measurements of cytosolic free calcium. *Cell Calcium* 11: 63–73 (1990)

55. Rudolf R, Mongillo M, Rizzuto R, Pozzan T: Looking forward to seeing calcium. *Nat Rev Mol Cell Biol* 4: 579–586 (2003)

56. Schaffer JL, Rizen M, L'Italien GJ, Benbrahim A, Megerman J, Gerstenfeld LC, Gray ML: Device for the application of a dynamic biaxially uniform and isotropic strain to a flexible cell culture membrane. *J Orthop Res* 12: 709–719 (1994)

57. Stroetz RW, Vlahakis NE, Walters BJ, Schroeder MA, Hubmayr RD: Validation of a new live cell strain system: characterization of plasma membrane stress failure. *J Appl Physiol* 90: 2361–2370 (2001)

58. Tschumperlin DJ, Margulies SS: Equibiaxial deformation-induced injury of alveolar epithelial cells in vitro. *Am J Physiol* 275: L1173–L1183 (1998)

59. Tschumperlin DJ, Margulies SS: Alveolar epithelial surface area-volume relationship in isolated rat lungs. *J Appl Physiol* 86: 2026–2033 (1999)

60. Tschumperlin DJ, Oswari J, Margulies AS: Deformation-induced injury of alveolar epithelial cells. Effect of frequency, duration, and amplitude. *Am J Respir Crit Care Med* 162: 357–362 (2000)

61. Tschumperlin DJ, Shively JD, Kikuchi T, Drazen JM: Mechanical stress triggers selective release of fibrotic mediators from bronchial epithelium. *Am J Respir Cell Mol Biol* 28: 142–149 (2003)

62. Vlahakis NE, Hubmayr RD: Invited review: plasma membrane stress failure in alveolar epithelial cells. *J Appl Physiol* 89: 2490–2496;discussion 2497 (2000)

63. Vlahakis NE, Hubmayr RD: Response of alveolar cells to mechanical stress. *Curr Opin Crit Care* 9: 2–8 (2003)

64. Wadsworth SJ, Spitzer AR, Chander A: Ionic regulation of proton chemical (pH) and electrical gradients in lung lamellar bodies. *Am J Physiol* 273: L427–L436 (1997)

65. Wang Y, Shyy JYJ, Chien S: Fluorescence proteins, live-cell imaging, and mechanobiology: seeing is believing. *Annu Rev Biomed Eng* 10: 1–38 (2008)

66. Waters CM, Glucksberg MR, Lautenschlager EP, Lee CW, Matre RMV, Warp RJ, Savla U, Healy KE, Moran B, Castner DG, Bearinger JP: A system to impose prescribed homogenous strains on cultured cells. *J Appl Physiol* 91: 1600–1610 (2001)

67. Wirtz HR, Dobbs LG: Calcium mobilization and exocytosis after one mechanical stretch of lung epithelial cells. *Science* 250: 1266–1269 (1990)

68. Wirtz HR, Dobbs LG: The effects of mechanical forces on lung functions. *Respir Physiol* 119: 1–17 (2000)

69. Wright JR, Clements JA: Metabolism and turnover of lung surfactant. *Am Rev Respir Dis* 136: 426–444 (1987)

70. Yavin E, Yavin Z: Attachment and culture of dissociated cells from rat embryo cerebral hemispheres on polylysine-coated surface. *J Cell Biol* 62: 540–546 (1974)

71. Yost MJ, Simpson D, Wrona K, Ridley S, Ploehn HJ, Borg TK, Terracio L: Design and construction of a uniaxial cell stretcher. *Am J Physiol Heart Circ Physiol* 279: H3124–H3130 (2000)

72. Zhuang J, Yamada KA, Saffitz JE, Kléber AG: Pulsatile stretch remodels cell-to-cell communication in cultured myocytes. *Circ Res* 87: 316–322 (2000)

Appendix A

Additional Results

In this chapter some additional results are shown for the individual strain protocols. Figures 28 and 29 show fusions detected by FM1-43 fluorescence and transient calcium peaks detected by Fura-2 fluorescence respectively. The figures show the relative number of cells responding with fusions and transient calcium peaks respectively plotted over time. Because of the low number of events per time period one has to be careful when trying to interpret the course of events over time.

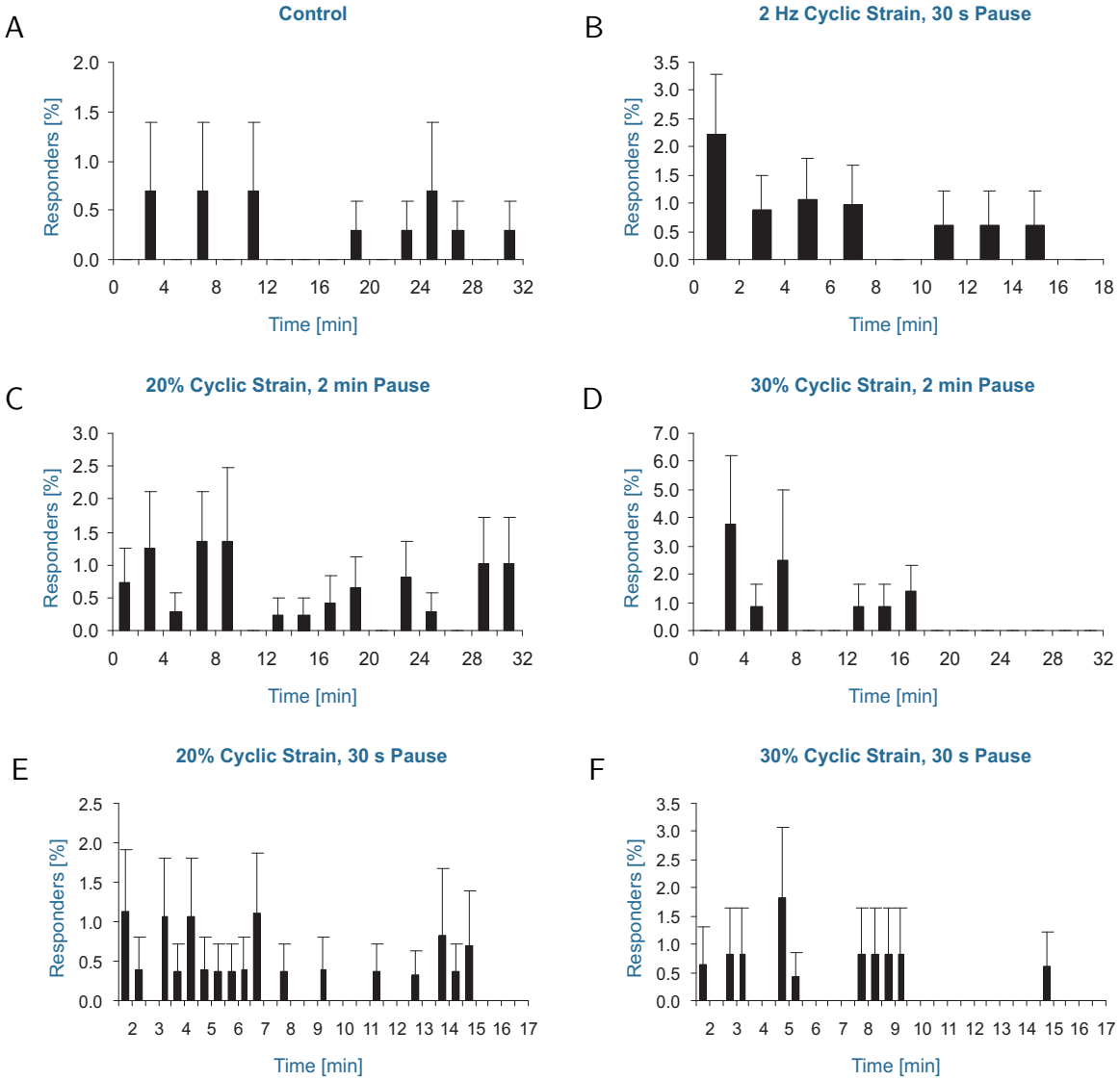

Figure 28 Lamellar body fusions over time shown per individual protocol. Fusions events were grouped by time (every 2 min, A) or by cycle (B-F). Bars represent mean percentage of cells exhibiting lamellar body fusions (plus standard error of mean).

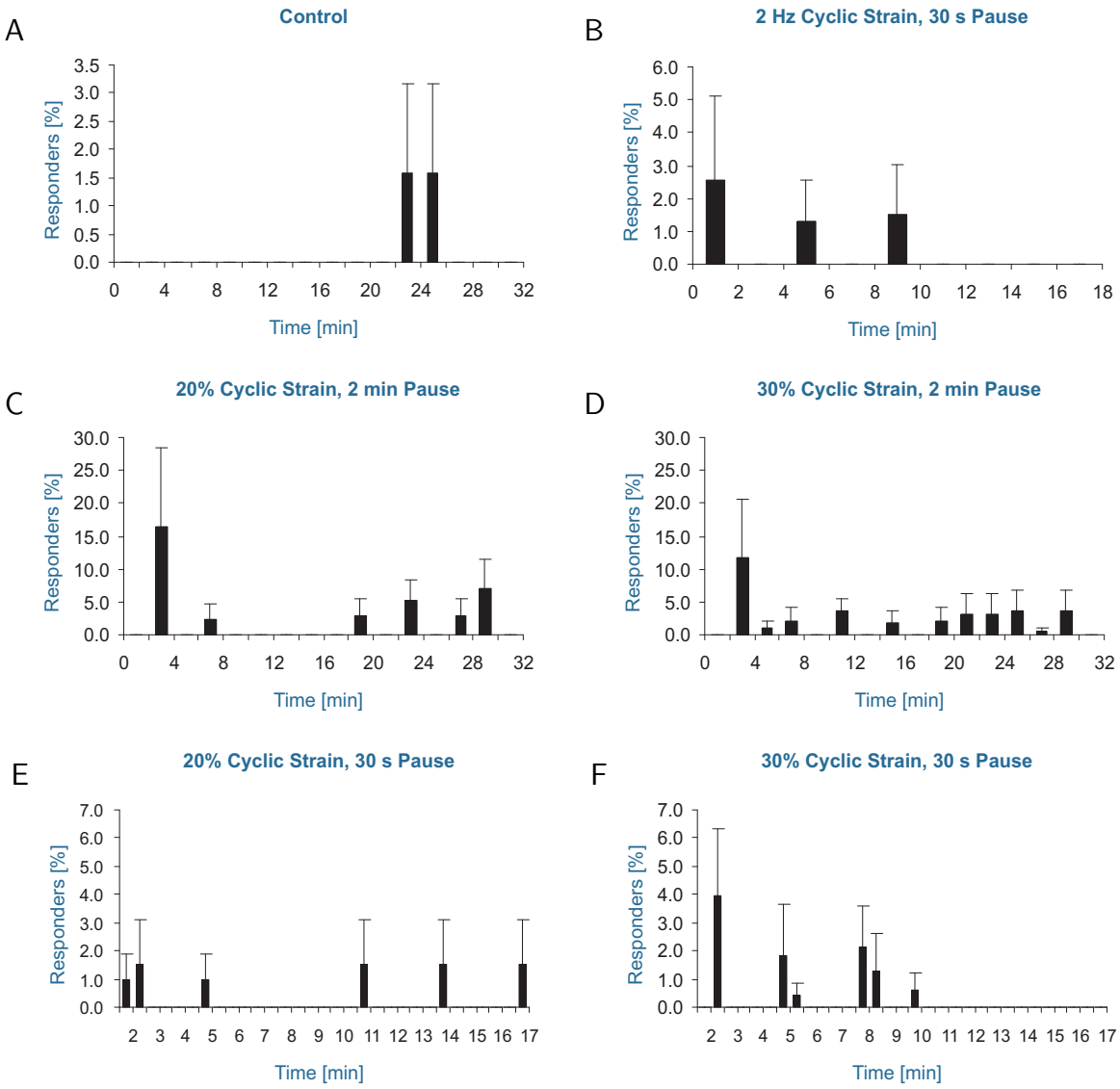

Figure 29 Transient calcium peaks over time shown per individual protocol. Calcium events were automatically detected as described in section 2.6.1 and grouped by time (every 2 min, A) or by cycle (B-F). Bars represent mean percentage of cells showing calcium peaks (plus standard error of mean).

Appendix B

Software Implementation

The strain control software (cf. section 2.2) has been implemented in C++ in a platform independent way relying heavily on the Qt application development framework from Trolltech. Currently, it runs only under Microsoft Windows®, a port for Apple Mac OS X®, however, is almost complete. Eclipse was used as the integrated development environment (IDE) and MinGW and GCC (under Windows and Mac OS X respectively) for compilation. Table 13 lists all used software components.

The software is broken down into two modules: the graphical user interface (GUI) module and the input/output (IO) module. The following sections describe each module in more detail.

Requirements

The following requirements must be met in order to run the strain control software:

- Microsoft Windows® XP
- a CPU with 1.5 GHz or more (a dual core processor is recommended)
- a RS-232 interface (serial port) or a USB adapter with a RS-232 interface

Table 13 Software and software components used for development

Software/Component	Location for more information
Eclipse IDE	`http://www.eclipse.org`
GCC, the GNU Compiler Collection	`http://gcc.gnu.org`
MinGW	`http://www.mingw.org`
Trolltech Qt	`http://trolltech.com/products/qt`

B.1 Graphical User Interface

Experiment Stores all settings specific to a single experiment. This class represents a container that stores all settings of an experiment, e.g. the warp profile and its parameters and the positions of the stage. The container is just a kind of map that stores key-value pairs. The data can be grouped in order to simplify organisation. The experiment can be saved as a file and then loaded again at a later time.

B.2 Device Control and Input/Output

Stage Controller Provides a programmatic interface to a motorized stage. A stage controller allows to query the current status of the attached stage, like its position, to move it to an absolute position or by a relative amount, and to set and query parameters like acceleration and maximum speed.

Warp Controller Provides access to a motorized strain/compression unit. A warp controller allows to apply strain to the attached membrane chamber and to query and set parameters like acceleration, maximum speed, prestrain. Additionally, it provides support for motion compensation.

Warp Profile Defines a function that describes how much strain has to be put on the strain/compression unit at a specific time point. A warp profile is composed of one or more warp segments that describe the change in strain over time in detail.

Warp Profile Runner Executes a warp profile by issuing appropriate commands to the warp and stage controller.

Warp Segment Defines a segment of a warp profile. A warp profile is composed of one or several warp segments. Segments always specify changes in strain as relative values so that they can be concatenated or repeated.

Motion Compensator Defines a function that describes how far to move the microscope stage to keep an observed position in place when applying a specific strain. When observing a point on the Cell Warp membrane through the microscope it will probably move out of the field of view when applying strain on the membrane (at least whenever the point is not the center of the membrane). Therefore, it is necessary to compensate for the movement by directing the microscope stage

in the opposite direction by the same distance and it will seem like the observed point staying at the same place. A motion compensator describes this correlation.

Serial Device Provides a programmatic interface to devices connected via a RS232 interface. A serial device facilitates input/output operations and allows to query and set parameters like baud rate, timeouts, and specific flags.

Acknowledgments

This research project would not have been possible without the support of many people.

First and foremost, I would like to express my deepest gratitude to Professor Dr. Paul Dietl for giving me the opportunity to work on an interdisciplinary project at his institute, supervising the project, having always an open door, and generously supporting me and my work for over two years.

I owe special thanks to Professor Dr. Anita Ignatius from the Institute of Orthopaedic Research and Biomechanics for spending her time on this thesis as second reviewer.

I would like to thank the whole team of the Institute of General Physiology for providing me with valuable scientific assistance and a great working atmosphere. Many thanks to Dr. Edward Felder and Dr. Oliver Wittekindt for many fruitful discussions and inputs, Dr. Pika Miklavc for reading and revising the thesis, Giorgio Fois for introducing me to the microscope setup and many routine tasks, our technicians Melanie Timmler and Tatiana Felder, and furthermore Susanne Albrecht, Ingrid Behr, Helga Brauchle, Ehrhard Schoch and everyone else in the institute.

My sincere gratitude goes also to my initial supervisor, Dr. Matthias Langer, who helped me in getting this project started, provided the necessary working environment, and assisted me with many technical and other questions. I also highly appreciate the support and technical assistance of François Grauvogel.

I would like to thank Siegfried Innerbichler for manufacturing the prototype of the cell strain device and helping to improve it, Dr. Wolfgang Singer for constructing the motion controller, and Herbert Schmitt for his design of the third generation membrane chambers.

Of course, my friends contributed a lot by their understanding and continuous motivation, which I'm deeply grateful for, in particular during the difficult times of the project. Many thanks especially to Jasmin Kuban.

Finally, I would like to thank my parents for always believing in me and supporting me in everything I do.

Axel Gerstmair, December 2008